


Longitudinal magnetoconductance and the planar Hall effect in a lattice model of tilted Weyl fermions

Azaz Ahmad  and Gargee Sharma*School of Basic Sciences, Indian Institute of Technology Mandi, Mandi 175005, India*

(Received 23 November 2020; accepted 17 March 2021; published 25 March 2021)

The experimental verification of chiral anomaly in Weyl semimetals is an active area of investigation in modern condensed matter physics, which typically relies on the combined signatures of longitudinal magnetoconductance (LMC) along with the planar Hall effect (PHE). It has recently been shown that for weak nonquantizing magnetic fields, a sufficiently strong finite intervalley scattering drives the system to switch the sign of LMC from positive to negative. Here we unravel another independent source that produces the same effect. Specifically, a smooth lattice cutoff to the linear dispersion, which is ubiquitous in real Weyl materials, introduces nonlinearity in the problem and also drives the system to exhibit negative LMC for noncollinear electric and magnetic fields even in the limit of vanishing intervalley scattering. We examine longitudinal magnetoconductivity and the planar Hall effect semianalytically for a lattice model of tilted Weyl fermions within the Boltzmann approximation. We independently study the effects of a finite lattice cutoff and tilt parameters and construct phase diagrams in relevant parameter spaces that are relevant for diagnosing chiral anomaly in real Weyl materials.

DOI: [10.1103/PhysRevB.103.115146](https://doi.org/10.1103/PhysRevB.103.115146)

I. INTRODUCTION

As dictated by the well-known no-crossing theorem [1], the Bloch bands in a solid typically do not cross each other at any point in the Brillouin zone. Some exceptions to this general rule are Dirac and Weyl materials, where nontrivial topology of the Bloch bands can stabilize the band-degenerate point [2–12]. In a Weyl semimetal (WSM), a band-crossing point, also known as a Weyl node, can act as a source or sink of Abelian Berry curvature [13]. Since the net Berry flux through the Brillouin zone must vanish, the Weyl nodes must occur in multiples of two. The topological nature of the Bloch bands in a WSM gives rise to very interesting physics typically that is absent in conventional condensed matter systems. Some examples include the manifestation of anomalous Hall [12, 14] and Nernst [15–17] effects, open Fermi arcs [10], and the most prominent one being the manifestation of chiral or Adler-Bell-Jackiw anomaly [18–27].

Weyl fermions have an associated chirality quantum number that is identical with the integral of the flux of the Berry curvature around a Weyl node. The number of Weyl fermions of a specific chirality remain conserved in the absence of an external gauge or gravitational field coupling. However, in the presence of background gauge fields, such as electric and magnetic fields, the separate number conservation laws for Weyl fermions are violated [18–20]. This is the result of chiral anomaly in Weyl fermions and has its origins rooted in high-energy physics. The verification of chiral anomaly in Weyl semimetals is an important area of investigation in condensed matter physics.

Chiral anomaly in WSMs may be verified by experimental probes such as that measure magnetoconductance [28–36], Hall effect [37–45], thermopower [15, 46–48], optical pro-

cesses [26, 49, 50], nonlocal transport [51], optical phonons [52–55]. It was initially concluded that chiral anomaly in WSMs directly correlates with the observation of positive longitudinal magnetoconductance (LMC). For example, from elementary field-theory calculations [27], the chiral chemical potential (μ_5 , which is the difference between the chemical potential between Weyl nodes of two chiralities) created by the external parallel \mathbf{E} and \mathbf{B} fields in the presence of intervalley scattering is $\mu_5 = 3v_F^3 e^2 \tau_i E B / 4\hbar^2 \mu^2$, where v_F , τ_i , and μ denote the Fermi velocity, scattering time, and the chemical potential, respectively. The corresponding longitudinal current is given by $j = e^2 \mu_5 B / 2\pi^2$, which immediately gives us positive longitudinal magnetoconductance. However, a detailed analysis shows that positive longitudinal magnetoconductance is neither a necessary nor a sufficient condition to prove the existence of chiral anomaly in WSMs. It has now been well established that both positive or negative magnetoconductance can arise from chiral anomaly in WSMs [56–73]. In the presence of strong magnetic field, when Landau quantization is relevant, the sign of magnetoconductance depends on the nature of scattering impurities [56–62]. For weak magnetic fields, it was recently shown that sufficiently strong intervalley scattering can switch the sign of LMC [71, 72].

In this work we unravel another independent source that produces negative LMC for weak noncollinear electric and magnetic fields even for vanishing intervalley scattering strength. Around a Weyl node, the energy dispersion locally behaves as $\epsilon_{\mathbf{k}}^x = \hbar v_F k$, where v_F is the Fermi velocity, while k is the modulus of the wave vector measured from the nodal point. In practice, the linear energy dispersion around a Weyl node is only valid for a small energy window. In a realistic lattice model of Weyl fermions, the bands are no longer linear far apart from the nodal point, and the lattice regularization

provides a physical ultraviolet cutoff to the low-energy spectrum. The lattice model of Weyl fermions introduces a source of nonlinearity in the problem and has important implications in several physical properties. For example, the lattice model of Weyl fermions produces a nonzero Nernst effect [15,16] (as also observed experimentally [17]), which is otherwise predicted to vanish in the linear approximation [46]. Here, we semianalytically examine longitudinal magnetoconductance and the planar Hall effect for a lattice model of Weyl fermions that has a smooth lattice cutoff. By a “smooth” lattice cutoff we mean that the dispersion gradually transitions from being linear to becoming flat at the corners of the Brillouin zone. This is in contrast to imposing a hard cutoff to the linear spectrum by discarding the high-energy contributions. The lattice model we adopt here is also advantageous over other continuum nonlinear models because (i) there is no need to impose a hard cutoff at higher energies, as the bands flatten out naturally at higher energies, (ii) includes nonlinearities up to all orders, and (iii) the expressions for Berry curvature and orbital magnetic moment in the current model offer better analytical tractability than some other nonlinear models. It is also worthwhile to point out that the lattice model we adopt has exact analytical expressions for the Berry curvature, orbital magnetic moment, and band velocities at all energies. This is in contrast to earlier works on a lattice model of Weyl semimetals mostly resorting to numerical evaluation of various intrinsic quantities such as the Berry curvature and the orbital magnetic moment, as well as transport quantities such as longitudinal conductance or the Hall conductance [15,16,25,37,70]. Therefore, in this work the associated transport quantities are also evaluated semianalytically within the Boltzmann formalism. Further, it is not straightforward to incorporate internode scattering in lattice models of a WSM because the energy dispersion valid throughout the first Brillouin zone does not “see” any distinction between nodes. In contrast, here we consider lattice models of individual Weyl nodes and thus it is straightforward to incorporate intervalley scattering akin to the case of two Weyl nodes with linearized dispersion.

We find that nonlinear lattice effects can produce negative LMC for noncollinear electric and magnetic fields even in the absence of intervalley scattering. Crucially, we note that it is important to account for orbital magnetic moment effects to obtain negative LMC. We also find that in the presence of finite intervalley scattering, lattice effects drive the system to exhibit negative longitudinal magnetoconductance quickly at a lesser threshold of intervalley scattering as compared to the linearized approximation.

Further, in realistic materials the Weyl cones not only have a smooth lattice cutoff, but are also in general tilted along a particular direction [70,74,75]. We also examine longitudinal magnetoconductance σ_{zz} and the planar Hall conductance σ_{xx} in the presence of a tilt parameter both parallel and perpendicular to the z direction. When the electric and magnetic fields are aligned parallel to each other, and when the Weyl cones are tilted along the direction of the magnetic field, LMC is quadratic if the cones are oriented in the same direction, and the sign of LMC depends on the strength of intervalley scattering (α_i). When the cones are tilted opposite to each other, LMC is found to be linear in B with sign depend-

ing on the magnitude of the tilt as well as α_i . When the cones are tilted perpendicular to the direction of the magnetic field, LMC is found to be quadratic, with the sign again depending on the value of intervalley scattering strength α_i . However, more interesting features emerge when LMC is examined for noncollinear electric and magnetic fields, as demonstrated by several phase plots in the α_i - t_k space (t_k being the tilt parameter). We also find that the planar Hall conductance also shows linear-in- B behavior for tilted Weyl cones oriented opposite to each other, and this linear-in- B behavior is enhanced in the presence of intervalley scattering α_i . Lastly, we also discuss the applicability of our results to a scenario more relevant to actual Weyl materials, i.e., the case of an inversion symmetry-broken Weyl semimetal by extending the Boltzmann formalism to tackle multiple nodes simultaneously. Interestingly, we find that despite the presence of internode scattering between nodes of opposite tilt orientation, the linear-in- B LMC coefficient vanishes for our model. We find that the interplay of various internode scattering channels along with the magnitude of tilt parameter governs the sign of LMC.

This paper is organized as follows: In Sec. II, we discuss the Boltzmann formalism for magnetotransport for a system of lattice Weyl nodes, that may also be tilted along a particular axis. Section III consists of our main results that are divided into four subsections as highlighted in Fig. 1. Finally, we conclude in Sec. IV. The technical details are relegated to the Appendices.

II. BOLTZMANN FORMALISM FOR MAGNETOTRANSPORT

We begin with the most general form of a tilted type-I Weyl node of a particular chirality χ , including nonlinear effects away from the Weyl node due to lattice regularization. The Hamiltonian expanded around each Weyl point can be expressed as

$$H_{\mathbf{k}} = \chi E_0 p(\mathbf{a}\mathbf{k} \cdot \boldsymbol{\sigma}) + T_x^\chi q(ak_x) + T_z^\chi r(ak_z). \quad (1)$$

In the above expression, E_0 is an energy parameter, T_x^χ and T_z^χ are tilt parameters along the x and z directions, respectively, \mathbf{k} is the momentum measured relative to the Weyl point, $\boldsymbol{\sigma}$ is the vector of the Pauli matrices. The functions p , q , and r can assume any form as long as $p(0) = q(0) = r(0) = 0$, but we choose $p(x) = q(x) = r(x) = \sin(x)$ as a prototype of a lattice Weyl node. The corresponding energy dispersion is given by

$$\epsilon_{\mathbf{k}}^\chi = \pm E_0 \sin(ka) + T_z^\chi \sin(ak_z) + T_x^\chi \sin(ak_x). \quad (2)$$

Note that for a Weyl node without any tilt, the energy bandwidth equals $2E_0$.

We study charge transport for weak electric and magnetic fields via the quasiclassical Boltzmann theory and thus the Landau quantization regime will not be relevant for our discussion. A phenomenological Boltzmann equation for the nonequilibrium distribution function $f_{\mathbf{k}}^\chi$ can be written as [76]

$$\left(\frac{\partial}{\partial t} + \dot{\mathbf{r}}^\chi \cdot \nabla_{\mathbf{r}} + \dot{\mathbf{k}}^\chi \cdot \nabla_{\mathbf{k}} \right) f_{\mathbf{k}}^\chi = \mathcal{I}_{\text{col}}[f_{\mathbf{k}}^\chi], \quad (3)$$

where the collision term on the right-hand side incorporates the effect of impurity scattering. In the presence of electric (\mathbf{E})

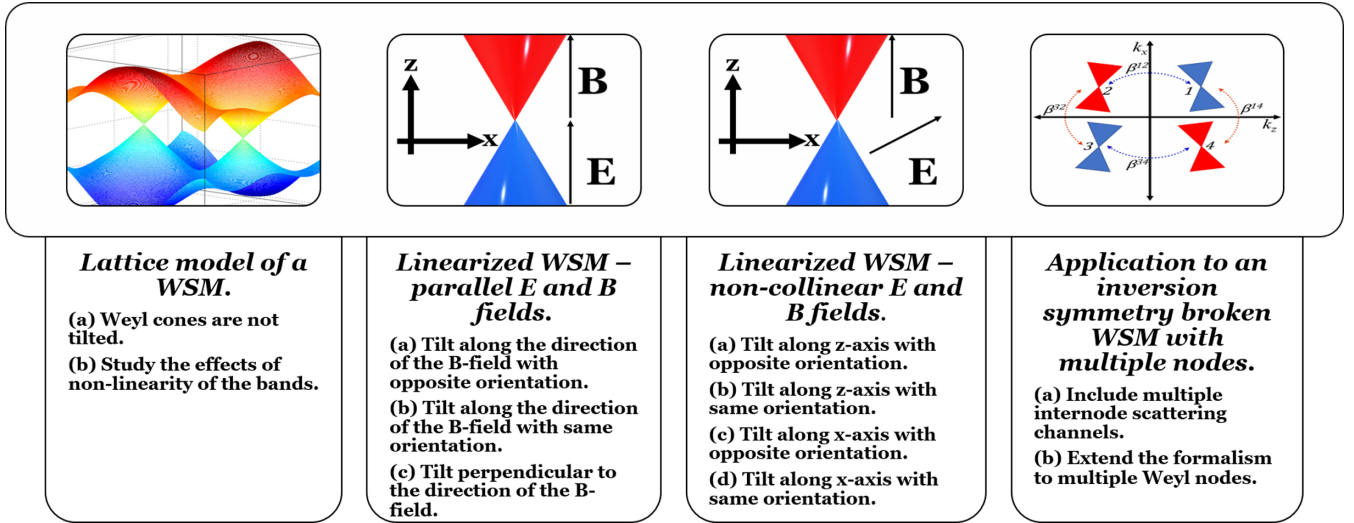


FIG. 1. Schematic of the presentation of results in Sec. III.

and magnetic (\mathbf{B}) fields, the dynamics of the Bloch electrons is modified as [24]

$$\begin{aligned}\dot{\mathbf{r}}^X &= \mathcal{D}^X \left[\frac{e}{\hbar} (\mathbf{E} \times \boldsymbol{\Omega}^X + \frac{e}{\hbar} (\mathbf{v}_k^X \cdot \boldsymbol{\Omega}^X) \mathbf{B} + \mathbf{v}_k^X) \right], \\ \dot{\mathbf{p}}^X &= -e\mathcal{D}^X (\mathbf{E} + \mathbf{v}_k^X \times \mathbf{B} + \frac{e}{\hbar} (\mathbf{E} \cdot \mathbf{B}) \boldsymbol{\Omega}^X),\end{aligned}\quad (4)$$

where \mathbf{v}_k^X is the band velocity, $\boldsymbol{\Omega}^X = -\chi \mathbf{k}/2k^3$ is the Berry curvature, and $\mathcal{D}^X = (1 + e\mathbf{B} \cdot \boldsymbol{\Omega}^X/\hbar)^{-1}$ is the factor by which the phase-space volume is modified due to Berry phase effects. The self-rotation of Bloch wave packet also gives rise to an orbital magnetic moment (OMM) [13] that is given by $\mathbf{m}_k^X = -e\chi E_0 \sin(ak) \mathbf{k}/2\hbar k^3$ for the above lattice model (see Appendix A for details). In the presence of magnetic field, the OMM shifts the energy dispersion as $\epsilon_k^X \rightarrow \epsilon_k^X - \mathbf{m}_k^X \cdot \mathbf{B}$. Note that the Berry curvature and the orbital magnetic moment are independent of the tilting of the Weyl cones.

The collision integral must take into account scattering between the two Weyl cones (internode, $\chi \iff \chi'$), as well as scattering within a Weyl cone (intranode, $\chi \iff \chi$), and thus $\mathcal{I}_{\text{col}}[f_k^X]$ can be expressed as

$$\mathcal{I}_{\text{col}}[f_k^X] = \sum_{\chi'} \sum_{\mathbf{k}'} W_{\mathbf{k}, \mathbf{k}'}^{\chi \chi'} (f_{\mathbf{k}'}^{\chi'} - f_{\mathbf{k}}^X), \quad (5)$$

where the scattering rate $W_{\mathbf{k}, \mathbf{k}'}^{\chi \chi'}$ in the first Born approximation is given by [76]

$$W_{\mathbf{k}, \mathbf{k}'}^{\chi \chi'} = \frac{2\pi}{\hbar} \frac{n}{\mathcal{V}} |\langle \psi_{\mathbf{k}'}^{\chi'} | U_{\mathbf{k}\mathbf{k}'}^{\chi \chi'} | \psi_{\mathbf{k}}^X \rangle|^2 \delta(\epsilon_{\mathbf{k}'}^{\chi'} - \epsilon_{\mathbf{k}}^X). \quad (6)$$

In the above expression n is the impurity concentration, \mathcal{V} is the system volume, $|\psi_{\mathbf{k}}^X\rangle$ is the Weyl spinor wave function [obtained by diagonalizing Eq. (1)], $U_{\mathbf{k}\mathbf{k}'}^{\chi \chi'}$ is the scattering potential profile, and ϵ_F is the Fermi energy. The scattering potential profile $U_{\mathbf{k}\mathbf{k}'}^{\chi \chi'}$ is determined by the nature of impurities (whether charged or uncharged or magnetic). Here we restrict our attention only to nonmagnetic pointlike scatterers, but particularly distinguish between intervalley and intravalley scattering that can be controlled independently in our formal-

ism. Thus, the scattering matrix is momentum independent but has a chirality dependence, i.e., $U_{\mathbf{k}\mathbf{k}'}^{\chi \chi'} = U^{\chi \chi'} \mathbb{I}$.

The distribution function is assumed to take the form $f_{\mathbf{k}}^X = f_0^X + g_{\mathbf{k}}^X$, where f_0^X is the equilibrium Fermi-Dirac distribution function and $g_{\mathbf{k}}^X$ indicates the deviation from equilibrium. In the steady state, the Boltzmann equation [Eq. (3)] takes the form

$$\begin{aligned}\left[\left(\frac{\partial f_0^X}{\partial \epsilon_{\mathbf{k}}^X} \right) \mathbf{E} \cdot \left(\mathbf{v}_{\mathbf{k}}^X + \frac{e\mathbf{B}}{\hbar} (\boldsymbol{\Omega}^X \cdot \mathbf{v}_{\mathbf{k}}^X) \right) \right] \\ = -\frac{1}{e\mathcal{D}^X} \sum_{\chi'} \sum_{\mathbf{k}'} W_{\mathbf{k}\mathbf{k}'}^{\chi \chi'} (g_{\mathbf{k}'}^{\chi'} - g_{\mathbf{k}}^X).\end{aligned}\quad (7)$$

The deviation $g_{\mathbf{k}}^X$ is assumed to be small such that its gradient can be neglected and is also assumed to be proportional to the applied electric field

$$g_{\mathbf{k}}^X = e \left(-\frac{\partial f_0^X}{\partial \epsilon_{\mathbf{k}}^X} \right) \mathbf{E} \cdot \boldsymbol{\Lambda}_{\mathbf{k}}^X. \quad (8)$$

We will fix the direction of the applied external electric field to be along $+\hat{z}$, i.e., $\mathbf{E} = E\hat{z}$. Therefore, only $\Lambda_{\mathbf{k}}^{Xz} \equiv \Lambda_{\mathbf{k}}^X$ is relevant. Further, we rotate the magnetic field along the xz plane such that it makes an angle γ with respect to the \hat{x} axis, i.e., $\mathbf{B} = B(\cos \gamma, 0, \sin \gamma)$. When $\gamma = \pi/2$, the electric and magnetic fields are parallel to each other. When $\gamma \neq \pi/2$, the electric and magnetic fields are noncollinear and this geometry will be useful in analyzing the planar Hall effect, as well as LMC in a noncollinear geometry that has nontrivial implications in a lattice model as well as for tilted Weyl fermions even in the linear approximation.

Keeping terms only up to linear order in the electric field, Eq. (7) takes the form

$$\mathcal{D}^X \left[v_{\mathbf{k}}^{Xz} + \frac{eB}{\hbar} \sin \gamma (\boldsymbol{\Omega}^X \cdot \mathbf{v}_{\mathbf{k}}^X) \right] = \sum_{\eta} \sum_{\mathbf{k}'} W_{\mathbf{k}\mathbf{k}'}^{\eta X} (\Lambda_{\mathbf{k}'}^{\eta} - \Lambda_{\mathbf{k}}^X). \quad (9)$$

In order to solve the above equation, we first define the valley scattering rate as follows:

$$\frac{1}{\tau_{\mathbf{k}}^{\chi}} = \nu \sum_{\eta} \int \frac{d^3 \mathbf{k}'}{(2\pi)^3} (\mathcal{D}_{\mathbf{k}'}^{\eta})^{-1} W_{\mathbf{k}\mathbf{k}'}^{\eta\chi}. \quad (10)$$

One would assume that when $\gamma = \pi/2$, due to the electric and magnetic field both being parallel to the \hat{z} axis the azimuthal symmetry is retained in the problem. However, due to the

tilting of the Weyl cones the azimuthal symmetry is destroyed even for parallel electric and magnetic fields, and therefore the above integration (and all other subsequent integrations) must be performed both over θ and ϕ when either (i) the Weyl cones are tilted and/or (ii) $\gamma \neq \pi/2$. Note that finite lattice effects by themselves do not break azimuthal symmetry. The radial integration is simplified due to the delta function in Eq. (6).

Substituting the scattering rate from Eq. (6) in the above equation, we have

$$\frac{1}{\tau_{\mathbf{k}}^{\chi}} = \frac{\nu N}{8\pi^2 \hbar} \sum_{\eta} |U^{\chi\eta}|^2 \iiint (k')^2 \sin \theta' \mathcal{G}^{\chi\eta}(\theta, \phi, \theta', \phi') \delta(\epsilon_{\mathbf{k}'}^{\eta} - \epsilon_F) (\mathcal{D}_{\mathbf{k}'}^{\eta})^{-1} dk' d\theta' d\phi', \quad (11)$$

where N now indicates the total number of impurities, and $\mathcal{G}^{\chi\eta}(\theta, \phi, \theta', \phi') = \{1 + \chi\eta[\cos \theta \cos \theta' + \sin \theta \sin \theta' \cos(\phi - \phi')]\}$ is the Weyl chirality factor defined by the overlap of the wave functions. Since quasiclassical Boltzmann theory is valid away from the nodal point such that $\mu^2 \gg \hbar v_F^2 eB$, therefore, without any loss of generality we will assume that the chemical potential lies in the conduction band.

Including orbital magnetic moment effects, the energy dispersion $\epsilon_{\mathbf{k}}^{\chi}$ is in general a function of several parameters including the chirality index, i.e., $\epsilon_{\mathbf{k}}^{\chi} = \epsilon_{\mathbf{k}}^{\chi}(E_0, k, a, \chi, B, \theta, \gamma)$. This equation has to be inverted in order to find a constant energy contour $k^{\chi} = k^{\chi}(E_0, \epsilon_{\mathbf{k}}^{\chi}, a, B, \theta, \gamma)$. For the case of lattice Weyl fermions, a closed-form analytical solution is not feasible and we will resolve to a numerical solution for k^{χ} . For tilted Weyl fermions in the linearized spectrum approximation, it is possible to invert the equation as will be shown shortly.

The three-dimensional integral in Eq. (11) is then reduced to just integration in ϕ' and θ' . The scattering time $\tau_{\mathbf{k}}^{\chi}$ depends on the chemical potential (μ), and is a function of the angular variables θ and ϕ :

$$\frac{1}{\tau_{\mu}^{\chi}(\theta, \phi)} = \nu \sum_{\eta} \iint \frac{\beta^{\chi\eta} (k')^3}{|\mathbf{v}_{\mathbf{k}'}^{\eta} \cdot \mathbf{k}^{\eta}|} \sin \theta' \mathcal{G}^{\chi\eta} (\mathcal{D}_{\mathbf{k}'}^{\eta})^{-1} d\theta' d\phi', \quad (12)$$

where the prefactor $\beta^{\chi\eta} = N|U^{\chi\eta}|^2/4\pi^2 \hbar^2$. The Boltzmann equation [Eq. (9)] assumes the form

$$\begin{aligned} h_{\mu}^{\chi}(\theta, \phi) + \frac{\Lambda_{\mu}^{\chi}(\theta, \phi)}{\tau_{\mu}^{\chi}(\theta, \phi)} \\ = \nu \sum_{\eta} \iint \frac{\beta^{\chi\eta} (k')^3}{|\mathbf{v}_{\mathbf{k}'}^{\eta} \cdot \mathbf{k}^{\eta}|} \sin \theta' \mathcal{G}^{\chi\eta} (\mathcal{D}_{\mathbf{k}'}^{\eta})^{-1} \Lambda_{\mu}^{\eta}(\theta', \phi') d\theta' d\phi'. \end{aligned} \quad (13)$$

We make the following ansatz for $\Lambda_{\mu}^{\chi}(\theta, \phi)$:

$$\begin{aligned} \Lambda_{\mu}^{\chi}(\theta, \phi) = [\lambda^{\chi} - h_{\mu}^{\chi}(\theta, \phi) + a^{\chi} \cos \theta \\ + b^{\chi} \sin \theta \cos \phi + c^{\chi} \sin \theta \sin \phi] \tau_{\mu}^{\chi}(\theta, \phi), \end{aligned} \quad (14)$$

where we solve for the eight unknowns ($\lambda^{\pm 1}, a^{\pm 1}, b^{\pm 1}, c^{\pm 1}$). The left-hand side in Eq. (13) simplifies to $\lambda^{\chi} + a^{\chi} \cos \theta + b^{\chi} \sin \theta \cos \phi + c^{\chi} \sin \theta \sin \phi$. The right-hand side of

Eq. (13) simplifies to

$$\begin{aligned} \nu \sum_{\eta} \beta^{\chi\eta} \iint f^{\eta}(\theta', \phi') \mathcal{G}^{\chi\eta} [\lambda^{\eta} - h_{\mu}^{\eta}(\theta', \phi') + a^{\eta} \cos \theta' \\ + b^{\eta} \sin \theta' \cos \phi' + c^{\eta} \sin \theta' \sin \phi'] d\theta' d\phi', \end{aligned} \quad (15)$$

where the function

$$f^{\eta}(\theta', \phi') = \frac{(k')^3}{|\mathbf{v}_{\mathbf{k}'}^{\eta} \cdot \mathbf{k}^{\eta}|} \sin \theta' (\mathcal{D}_{\mathbf{k}'}^{\eta})^{-1} \tau_{\mu}^{\chi}(\theta', \phi'). \quad (16)$$

The above equations, when written explicitly, take the form of seven simultaneous equations to be solved for eight variables (see Appendix B for details). The last constraint comes from the particle-number conservation

$$\sum_{\chi} \sum_{\mathbf{k}} g_{\mathbf{k}}^{\chi} = 0. \quad (17)$$

Thus, Eqs. (14)–(17) can be solved together with Eq. (12), simultaneously for the eight unknowns ($\lambda^{\pm 1}, a^{\pm 1}, b^{\pm 1}, c^{\pm 1}$). Due to the complicated nature of the problem, the associated two-dimensional integrals with respect to $\{\theta', \phi'\}$, and the solution of the simultaneous equations are all performed numerically. Before we proceed further, we will divide our results into two broad classes. The first class considers the effects of introducing a natural lattice cutoff for Weyl fermions without considering tilting of the Weyl cones. In the second class, we consider effects due to tilting the Weyl cones in the linearized spectrum approximation, that is without considering effects due to a finite lattice cutoff. Although our formalism can handle the generic case of tilted lattice Weyl fermion, the reason for this division is because effects due to lattice and due to tilting of the Weyl cones can in fact be considered independent of each other, and linearized approximation speeds up the numerical computation. The combined effect from the two gives the net result.

A. Noncollinear E and B fields without tilting of the Weyl cones for lattice Weyl fermions

Including orbital magnetic moment effects, the energy dispersion assumes the form of the following transcendental equation

$$\begin{aligned} 2\hbar k^2 \epsilon_k^{\chi} = 2\hbar k^2 E_0 \sin(ka) + e\chi E_0 \sin(ak) B [\cos(\theta) \sin \gamma \\ + \sin \theta \cos \phi \cos \gamma]. \end{aligned} \quad (18)$$

The above equation has no closed-form solution for the momentum k^x , and therefore the constant Fermi energy contour in k space is evaluated numerically. The semiclassical band velocities evaluated in spherical polar coordinates are

$$\begin{aligned} v_k^x &= \frac{E_0 a \cos(ak)}{\hbar} - \frac{u_2^x \cos(ak) \beta_{\theta\phi}}{\hbar a k^2} + \frac{2u_2^x \sin(ak) \beta_{\theta\phi}}{\hbar a^2 k^3}, \\ v_{\theta}^x &= \frac{u_2^x \sin(ak) (-d\beta_{\theta\phi}/d\theta)}{\hbar a^2 k^3}, \quad v_{\phi}^x = \frac{u_2^x (-d\beta_{\theta\phi}/d\phi)}{\hbar a^2 k^3 \sin \theta}, \\ u_2^x &= -e\chi E_0 B a^2 / 2\hbar, \end{aligned} \quad (19)$$

where $\beta_{\theta\phi} = (\sin \theta \cos \phi \cos \gamma + \cos \theta \sin \gamma)$.

B. Noncollinear E and B fields with tilting of the Weyl cones in the linear approximation

Since tilting and lattice cutoff effects are physically independent of each other, we treat these effects separately. Linearizing the Hamiltonian in Eq. (1) around the nodal point, we obtain

$$H_{\mathbf{k}} = \chi \hbar v_F \mathbf{k} \cdot \boldsymbol{\sigma} + t_x^x k_x + t_z^x k_z, \quad (20)$$

where we define $v_F = aE_0/\hbar$, $t_i^x = T_i^x a$. The expression for the constant energy contour becomes

$$k^x = \frac{\epsilon_{\mathbf{k}}^x + \sqrt{(\epsilon_{\mathbf{k}}^x)^2 - l^x \chi \xi e v_F B \beta_{\theta\phi}}}{l^x}, \quad (21)$$

where $l^x = 2\hbar v_F + 2t_x^x \cos \theta + 2t_z^x \sin \theta \cos \phi$, while the semiclassical velocities take the following form:

$$\begin{aligned} v_x^x &= v_F \frac{k_x}{k} + \frac{t_x^x}{\hbar} + \frac{v_2^x}{k^2} \left[\cos \gamma \left(1 - \frac{2k_x^2}{k^2} \right) - \frac{2 \sin \gamma k_x k_z}{k^2} \right], \\ v_y^x &= v_F \frac{k_y}{k} + \frac{v_2^x}{k^2} \left[\cos \gamma \left(\frac{-2k_x k_y}{k^2} \right) + \sin \gamma \left(\frac{-2k_y k_z}{k^2} \right) \right], \\ v_z^x &= v_F \frac{k_z}{k} + \frac{t_z^x}{\hbar} + \frac{v_2^x}{k^2} \left[\frac{-2 \cos \gamma k_x k_z}{k^2} + \sin \gamma \left(1 - \frac{2k_z^2}{k^2} \right) \right], \\ v_2^x &= \frac{\chi e v_F B}{2\hbar}. \end{aligned} \quad (22)$$

III. RESULTS

We now present our main results in a format as schematically presented in Fig. 1.

A. LMC for lattice Weyl semimetal in the absence of tilt

We first discuss the results for the lattice model of a Weyl semimetal without considering the effects of tilting of the Weyl cones. Since the effects of tilting of the Weyl cones are independent of lattice effects, tilting of the Weyl cones will be considered subsequently. The obtained LMC is found to be quadratic in magnetic field, and thus we expand the LMC as $\sigma_{zz}(B) = \sigma_{zz0} + \sigma_{zz2} B^2$. The linear-in- B term σ_{zz1} , which is zero here will become crucial for our analysis when we introduce tilting of Weyl fermions, as discussed later on. The longitudinal magnetoconductance switches sign from positive to negative at a critical value of $\alpha_i^c(\gamma, E_F)$, i.e., the coefficient σ_{zz2} becomes negative when $\alpha_i > \alpha_i^c(\gamma, E_F)$ as shown in Figs. 2(a)–2(c). At a fixed relative orientation of the magnetic

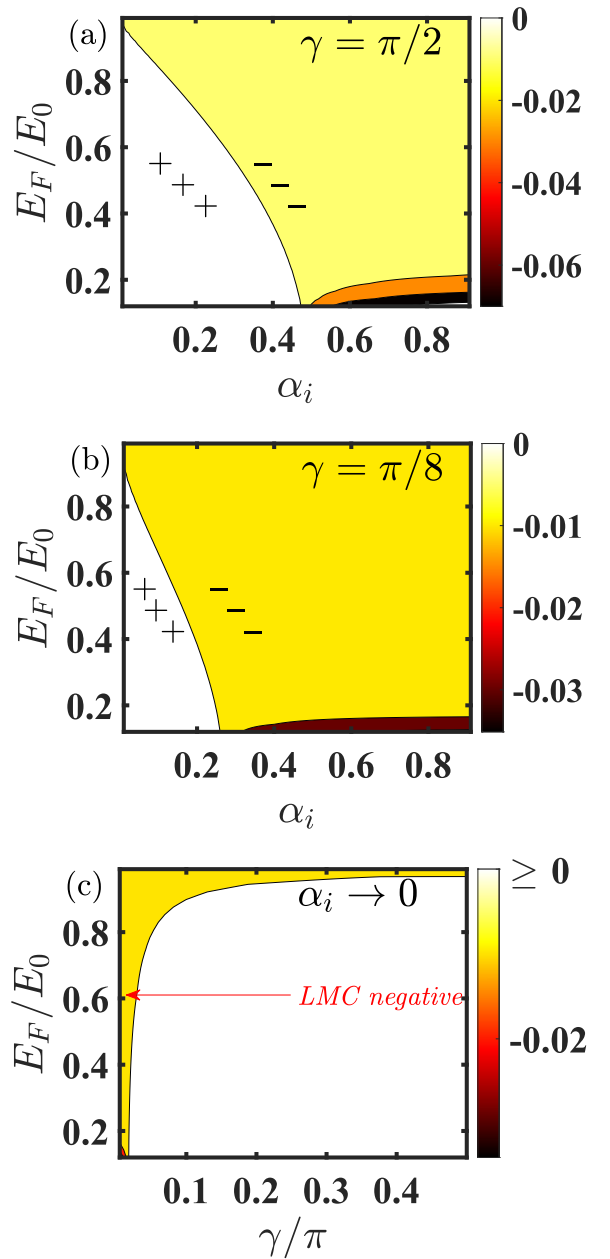


FIG. 2. (a)–(c) Phase plot of the quadratic coefficient of the longitudinal magnetoconductance for a lattice model of untilted Weyl fermions as a function of Fermi energy and intervalley scattering strength α_i for various different angles of the magnetic field. We explicitly map the zero-LMC contour in the $E_F - \alpha_i$ space where the change in sign of LMC occurs. At higher Fermi energies, the switching of LMC sign from positive to negative happens at a lower threshold of $\alpha_i = \alpha_i^c$ due to nonlinear lattice effects. Second, orienting the magnetic field direction away from the electric field also lowers the threshold value of α_i^c . (d) Quadratic LMC coefficient in the limit of vanishing intervalley scattering strength α_i as a function of the Fermi energy and angle of the magnetic field.

field (γ), the threshold of α_i^c decreases as the Fermi energy is increased.

Within the linear approximation of a Weyl cone one obtains straight-line contour separating positive and negative LMC areas with a constant α_i^c as a function of E_F instead of a curved

contour. Nonlinear lattice effects lower the critical value of α_i^c highlighting the fact that lattice effects can assist driving the system to exhibit negative LMC. The explicit zero-LMC contour plotted in Fig. 2 separates positive and negative LMC regions.

A very interesting feature emerges when the magnetic field is oriented further away from the electric field, in which case the α_i becomes smaller. Now, from Figs. 2(a)–2(c), we note that even when $\alpha_i = 0$, i.e., in the absence of any intervalley scattering, there is an upper energy cutoff beyond which LMC becomes negative. This feature is specifically highlighted in Fig. 2(d) where we plot σ_{zz} as a function of E_F and angle γ , in the limit of vanishing intervalley scattering strength α_i . This feature specifically points out the fact that lattice effects in Weyl fermions can *independently* produce negative LMC even in the absence of a finite intervalley scattering, a previously unknown result. For parallel electric and magnetic fields, the LMC is primarily positive even when lattice effects start to become important and becomes negative only at very high Fermi energies near the band edge. When the magnetic field is oriented away from the electric field, even small nonlinear lattice effects can produce negative LMC. As one would expect, the nonlinear effects matter more (less) when the Fermi energy is farther away (nearer) from the Weyl nodes because conductivity is essentially a Fermi surface quantity. We recover this result of linearized dispersion [73] in the limit $E_F \ll E_0$.

The planar Hall effect on the other hand does not display any sign change due to nonlinear lattice effects and displays the standard $\sin(2\gamma)$ trend as a function of the angle γ . Thus, we do not explicitly plot this behavior. PHE will be discussed in detail for tilted Weyl fermions subsequently.

B. LMC in tilted Weyl semimetal for parallel electric and magnetic fields

First, we discuss the case of tilted Weyl fermions when the electric and magnetic fields are held parallel to each other, i.e., $\gamma = \pi/2$. In this case the PHE contribution is expected to vanish and hence only LMC is discussed.

1. Weyl cones tilted along the magnetic field direction with opposite orientation

Figure 3 presents the results of LMC $\sigma_{zz}(B)$ as a function of magnetic field when the two Weyl cones are tilted along the direction of the magnetic field but oriented opposite to each other, i.e., $t_z^1 = -t_z^{-1}$, and $t_x^1 = 0$. In the absence of any intervalley scattering and tilt, the LMC is always positive, quadratic in the magnetic field, and symmetric about $B = 0$ as expected. Now, retaining the intervalley scattering to be zero, a finite tilt introduces a linear-in- B term in the LMC and thus also introduces a corresponding asymmetry around $B = 0$, i.e., now the value of the magnetoconductance depends on the direction of magnetic field, or more generally it is dependent on the orientation of the magnetic field with respect to the direction of the tilt. Note that the B -linear term survives because the tilts of the Weyl cones are opposite to each other. For higher tilt values ($\sim \geq 0.4$) the linear-in- B term dominates over the quadratic term and the LMC is observed to be linear in the relevant range of the magnetic field.

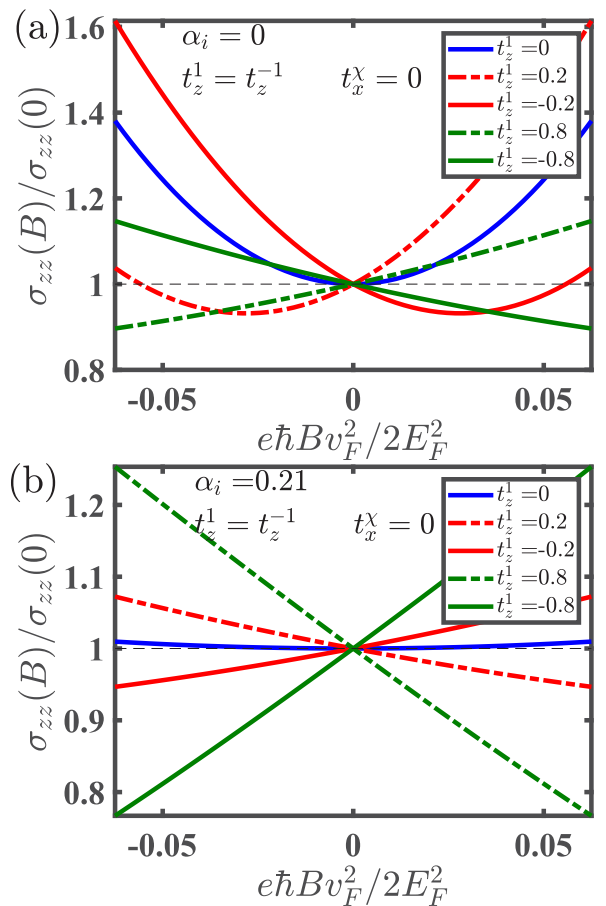


FIG. 3. Longitudinal magnetoconductance $\sigma_{zz}(B)$ in the case when the Weyl cones are tilted in the direction of the magnetic field (\hat{z} axis), but are oriented opposite to each other ($t_z^1 = -t_z^{-1}$). (a) LMC as a function of magnetic field for various tilt parameters in the absence of intervalley scattering ($\alpha_i = 0$). For a finite small tilt t_z^1 the LMC is asymmetric about zero magnetic field, but still appears to be quadratic. When the tilt is large, LMC is predominantly linear in B , (b) LMC in the presence of a finite intervalley scattering α_i .

In the presence of finite intervalley scattering, there is a qualitative change in the behavior of LMC, i.e., above a critical value $\alpha_i^c(t_z^1)$, LMC switches sign from positive to negative. In order to better understand this behavior, we expand the longitudinal magnetoconductance as $\sigma_{zz}(B) = \sigma_{zz0} + \sigma_{zz1}B + \sigma_{zz2}B^2$, where each coefficient σ_{zzj} corresponds to the j th order in the magnetic field. The calculated LMC as a function of the magnetic field is then fit according to the above equation to obtain the coefficients σ_{zzj} . The linear and quadratic coefficients are plotted in Fig. 4. For small intervalley scattering strength the linear and quadratic coefficients are similar in their magnitude, and therefore the behavior with respect to the magnetic field has an overall quadratic trend. When α_i crosses threshold value α_i^c , the linear coefficient dominates and LMC switches sign as a function of the magnetic field. Note that in the absence of any tilt, the linear coefficient is always zero and the LMC switches sign when $\alpha_i = 0.5$ [73]. However, for even small values of t_z^1 , the linear coefficient dominates over the quadratic coefficient and the sign reversal in LMC occurs below $\alpha_i = 0.5$.

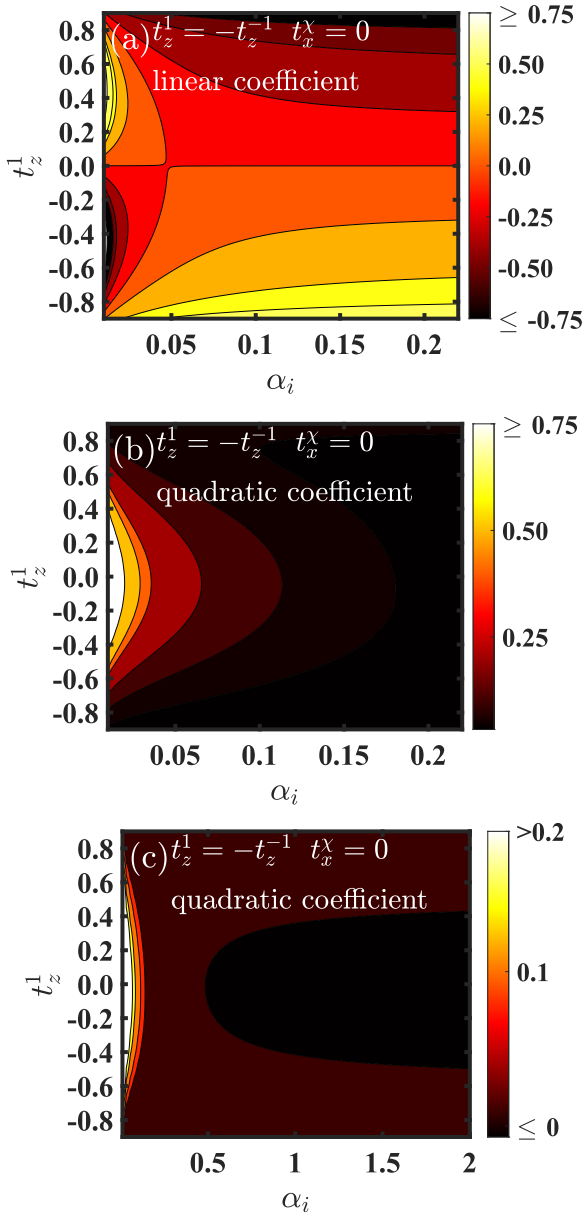


FIG. 4. (a), (b) Linear (σ_{zz1}) and quadratic (σ_{zz2}) coefficient of the LMC when the Weyl cones are tilted in the direction of the magnetic field (\hat{z}) axis, but are oriented opposite to each other ($t_z^1 = -t_z^{-1}$). Below $\alpha_i \sim 0.05$, the coefficients are similar in magnitude and LMC has an overall quadratic trend. For large enough α_i , the linear coefficient dominates over the quadratic coefficient leading to an overall linear-in- B LMC as well as a change in sign of LMC. (c) Quadratic coefficient over a larger range exhibiting a change of sign.

2. Weyl cones tilted along the magnetic field with same orientation

Figure 5 presents the results of LMC as a function of magnetic field when the two Weyl cones are tilted in the same direction with respect to each other in the direction of the magnetic field, i.e., $t_z^1 = t_z^{-1}$, and $t_x^1 = 0$. We first note that LMC is always quadratic in B because the B -linear coefficients cancel out (as they appear with a chirality sign that is opposite for the two Weyl cones). When the intervalley scattering strength is small, LMC is always positive, however, for large intervalley

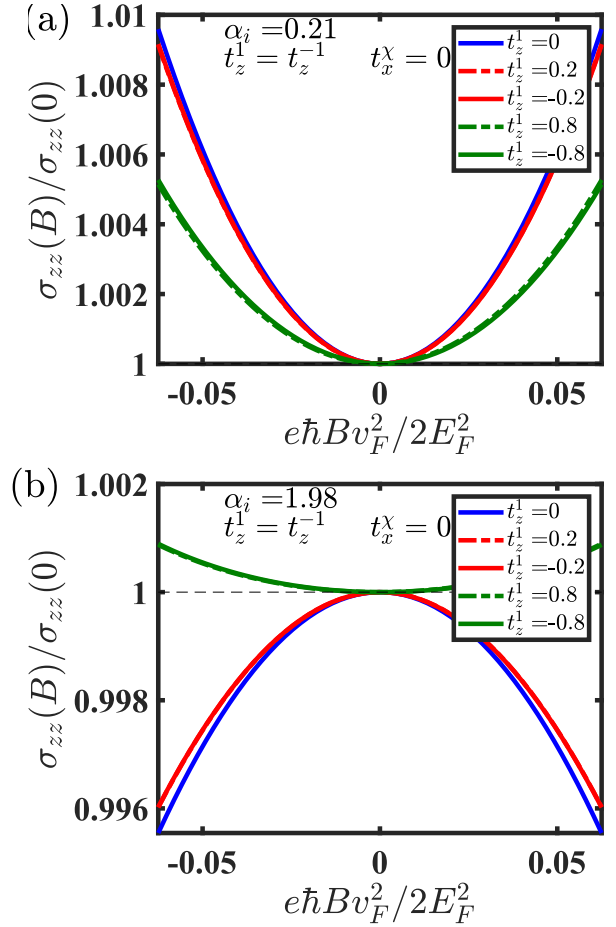


FIG. 5. Longitudinal magnetoconductance $\sigma_{zz}(B)$ in the case when the Weyl cones are tilted in the direction of the magnetic field (\hat{z}) axis, and are oriented in the same direction to each other ($t_z^1 = t_z^{-1}$). LMC switches sign with the inclusion of α_i whenever $\alpha_i > \alpha_i^c(t_z)$.

strength the behavior depends on the relative magnitude of the tilt parameter. If the magnitude of the tilt is small, the magnetoconductance switches sign, but this is opposed for large enough values of the tilt parameter.

In Fig. 6 we present the phase plot of the quadratic coefficient σ_{zz2} . The sign of the quadratic coefficient corresponds to the sign of LMC in this case as the linear-in- B term is absent. We also map out the contour in $\alpha_i - t_z^1$ space where the change in sign of LMC occurs. When $\alpha_i \gtrsim 0.5$ and $|t_z^1| \lesssim 0.6$, LMC is observed to be negative, but remains positive and has a weak dependence on α_i when $|t_z^1| \gtrsim 0.6$. The LMC is determined by the interplay of α_i and t_z^1 and the tilt parameter opposes the change in sign of LMC due to intervalley scattering and its contribution dominates when $|t_z^1| \gtrsim 0.6$.

3. Weyl cones tilted perpendicular to the magnetic field

When the Weyl cones are tilted orthogonal to the direction of the magnetic field, i.e., $t_x^1 = \pm t_x^{-1} \neq 0$ and $t_z^1 = 0$, we find the qualitative trend is very similar to the previously discussed case of $t_x^1 = 0$ and $t_z^1 = t_z^{-1} \neq 0$. Due to the qualitative similarities with Figs. 5 and 6, we do not explicitly plot the behavior.

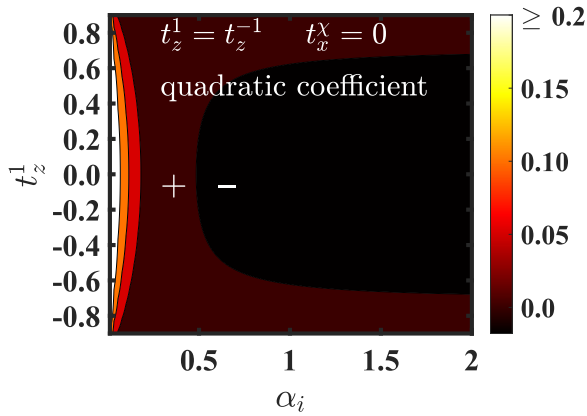


FIG. 6. The quadratic coefficient of LMC is plotted as a function of α_i and t_z^1 when the Weyl cones are tilted in the direction of the magnetic field (\hat{z}) axis, and are oriented in the same direction to each other ($t_z^1 = t_z^{-1}$). The sign of the coefficient also corresponds to the sign of LMC. The contour separating positive and negative LMC regions is also clearly shown.

C. LMC in tilted Weyl semimetal for noncollinear electric and magnetic fields

Naively, one would expect that the longitudinal magnetoconductance will be qualitatively similar for noncollinear fields to collinear electric and magnetic fields. However, there are certain subtle nontrivial features that emerge. We will discuss each of these below.

1. Weyl cones tilted along the z axis with same orientation

For the same orientation of the Weyl cones, the linear-in- B contribution to the LMC is absent. Thus, the sign of the quadratic coefficient corresponds to the sign of LMC. One would therefore expect that the qualitative behavior in this case would again be similar to that observed in Fig. 5, however, we find that this is not the case. In Fig. 7 we plot the sign of LMC as a function of the tilt t_z^1 and intervalley scattering α_i for a particular orientation of noncollinear electric and magnetic fields.

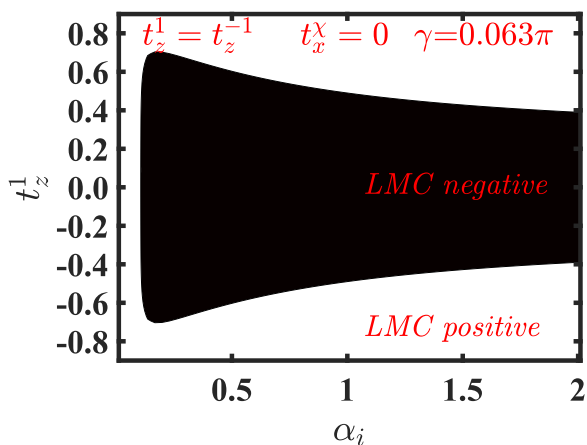


FIG. 7. The sign of longitudinal magnetoconductance for noncollinear fields as a function of intervalley scattering strength and tilt parameter, when the cones are tilted along the same direction parallel to the z axis.

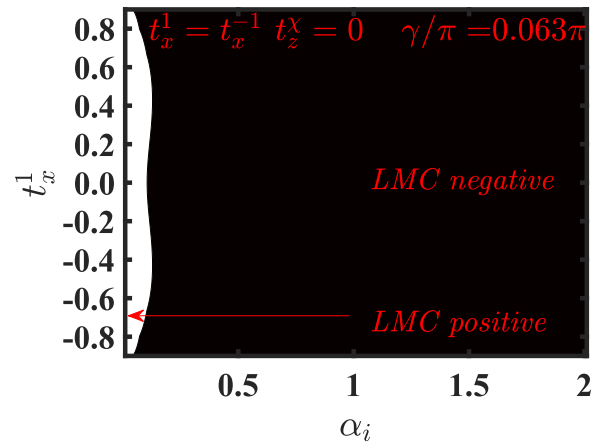


FIG. 8. The sign of longitudinal magnetoconductance for noncollinear fields as a function of intervalley scattering strength and tilt parameter, when the cones are tilted along the same direction parallel to the x axis.

As $\gamma \rightarrow \pi/2$ (parallel \mathbf{E} and \mathbf{B} fields), we recover the result presented in Fig. 5, i.e., the shape of zero-LMC contour resembles a U (as in Fig. 7). Specifically, when $|t_z^1| \lesssim 0.6$ critical value of α_i where the sign change occurs is around 0.5. When γ is directed away from $\pi/2$ the shape of the zero LMC contour looks like a curved trapezoid instead of U . The evolution from one to the other can be noted in Appendix C. This feature can be understood as a combination of two factors: for parallel field configuration, finite tilt and intervalley scattering drives the system to change the sign of LMC from positive to negative (as seen in Fig. 5), and second for noncollinear fields along with a finite α_i (even when $t_z^1 = 0$) drives the system to change LMC sign from positive to negative at a lower critical intervalley scattering strength [73]. The combination of these two assisting factors shapes the zero LMC contour in the current scenario.

2. Weyl cones tilted along the x axis with same orientation

From the previous discussions, it is suggested that the qualitative behavior of LMC for the three scenarios (a) $\{t_z^1 = t_z^{-1} \neq 0, t_x^x = 0\}$, (b) $\{t_x^1 = t_x^{-1} \neq 0, t_z^x = 0\}$, and (c) $\{t_x^1 = -t_x^{-1} \neq 0, t_z^x = 0\}$ is similar to each other for collinear electric and magnetic fields. Therefore, rotating the magnetic field along the xz plane (shifting γ away from $\pi/2$) is not expected to change any qualitative behavior. On the contrary, we find that this is not the case. Let us focus on cases (a) and (b). The qualitative similarity for parallel electric and magnetic fields is given by the following properties: (i) LMC is quadratic in B , (ii) LMC switches sign from positive to negative above a critical intervalley scattering strength, (iii) LMC always remains positive if the tilt parameter is above a critical tilt value ($\gtrsim 0.6$), as also suggested by the shape of zero-LMC contour (U shaped). When the fields are not parallel, then in case (a) the zero-LMC contour assumes the form of a curved trapezoid (Fig. 7). The corresponding contour for the present case (b) assumes a different form as seen in Fig. 8. In this case, the region of negative LMC expands in the parameter space along with the reduction of the critical intervalley strength. The reduction of the critical intervalley strength can again be

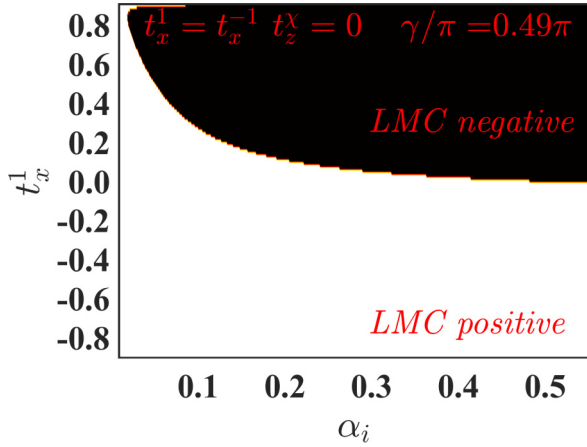


FIG. 9. LMC for noncollinear electric and magnetic fields when the Weyl cones are tilted along the x axis and oppositely oriented to each other. A finite tilt is noted to result in a small linear-in- B contribution that enhances in the presence of intervalley scattering. The sign of LMC shows a striking change compared to Fig. 6.

understood as a combination of the two factors like in the previous case (i) finite tilt and intervalley scattering drives the system to change the LMC sign from positive to negative, and second when the fields are noncollinear, finite intervalley scattering independently drives the system to change LMC sign from positive to negative much below. The different shape of the contour (negative LMC filling out the parameter space instead of assuming a curved trapezoid) is essentially because the cones are now tilted along the x direction and the magnetic field has an x component to it, which is qualitatively different from the tilt occurring in the z direction. The complete evolution can be noted in Appendix C.

3. Weyl cones tilted along the x axis with opposite orientation

In Sec. III B we noted that when the Weyl cones are tilted perpendicular to the magnetic field axis, the qualitative behavior is independent of their mutual orientation. We find that when the field acquires even a small component along the direction of the tilt axis, the qualitative behavior of the LMC is strikingly different for different mutual orientations. Directing the magnetic field even slightly away from the z axis changes the qualitative behavior when $t_x^1 = -t_x^{-1}$, as a B -linear component is added in the LMC response. This is because the magnetic field now has an x component and the tilts are oppositely oriented to each other (though tilted along the x axis). Figure 9 presents the plot of LMC σ_{zz} as a function of the magnetic field when the angle of the magnetic field is slightly shifted away from the direction of the magnetic field. A finite tilt results in a small linear-in- B contribution that is enhanced in the presence of intervalley scattering. The complete evolution is plotted in Appendix C.

D. PHC in tilted Weyl semimetals for noncollinear electric and magnetic fields

1. Weyl cones tilted along the z axis with opposite orientation

As mentioned earlier, planar Hall conductance will be nonzero when the electric and magnetic field are not parallel

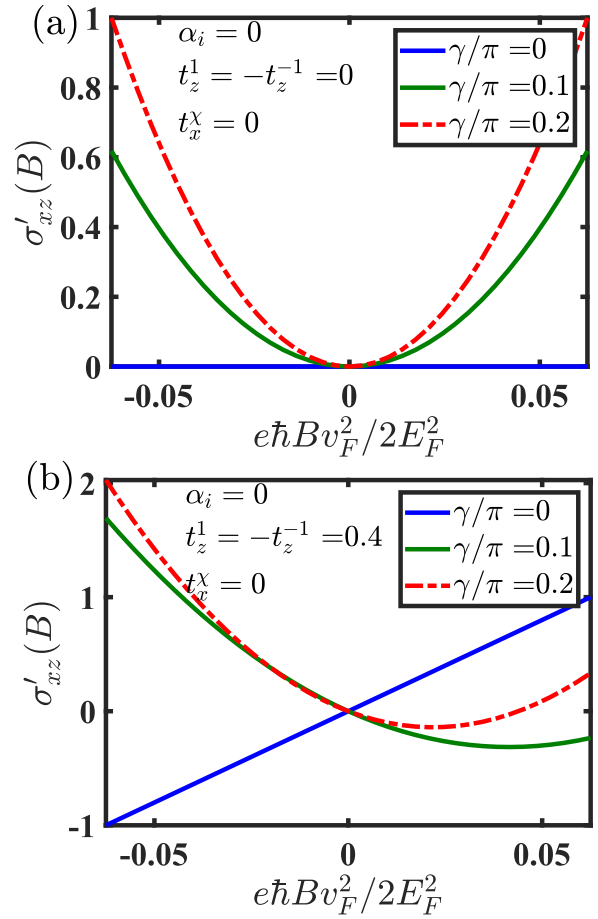


FIG. 10. Normalized planar Hall conductivity σ'_{xz} (prime indicating that the value is normalized with respect to the value at 0.5 T) as a function of the magnetic field for different values of the tilt parameter t_z^x (oppositely tilted Weyl cones) and at angles γ . A finite tilt is observed to add a B -linear component that shifts the minima of σ'_{xz} away from $B = 0$. For a higher tilt value, the behavior is linear for all relevant range of magnetic field.

to each other. In Figs. 10 and 11 we plot the normalized planar Hall conductivity σ'_{xz} as a function of the magnetic field for different values of the tilt parameter t_z^x for oppositely tilted Weyl cones. In the absence of intervalley scattering strength, a finite tilt is observed to add a B -linear component that shifts the minimum of the conductivity away from $B = 0$. For higher values of tilt, the behavior is almost linear for all relevant ranges of magnetic field. On the other hand, a finite intervalley strength α_i enhances the B -linear contribution, however, only for tilted Weyl fermions. In Appendix D, we plot the normalized planar Hall conductivity (σ'_{xz}) as a function of the angle γ for several values of tilt parameter t_z for oppositely tilted Weyl cones.

2. Weyl cones tilted along the x axis with opposite orientation

Figure 12 plots the normalized planar Hall conductance σ'_{xz} as a function of the magnetic field. Even in the absence of intervalley scattering, a finite tilt of the Weyl cones along the x direction causes the planar Hall conductivity to be linear in the magnetic field showing an asymmetry

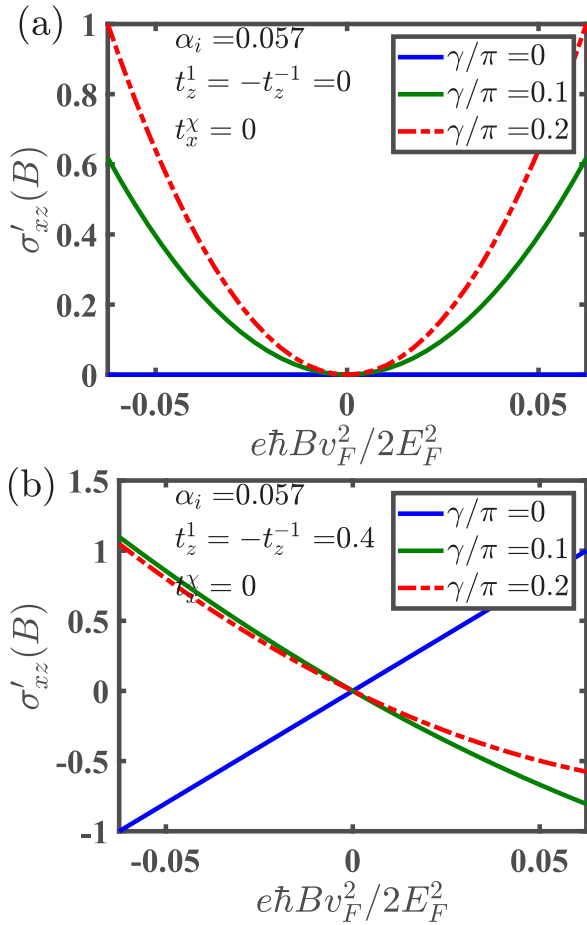


FIG. 11. Normalized planar Hall conductivity σ'_{xz} (prime indicating that the value is normalized with respect to the value at 0.5 T) as a function of the magnetic field for different values of the tilt parameter t_z^x (oppositely tilted Weyl cones) and at angles γ . A finite intervalley scattering strength α_i enhances the B -linear contribution, however, only in the presence of a finite tilt.

around $B = 0$. The presence of intervalley scattering further enhances the B -linear contribution as shown in Fig. 13. A subtle but yet important difference between this and the previous case is that in the current scenario, the planar Hall conductivity remains zero when $\gamma = 0$, i.e., when the magnetic field points along the x direction because the direction is parallel with the direction of tilts in the Weyl cone. On the other hand, when $\gamma = 0$, the planar Hall conductivity becomes finite and linear when the Weyl cones are tilted along the z direction. This point is explicitly highlighted in Appendix D, where we plot σ'_{xz} as a function of γ .

E. LMC in an inversion symmetry-broken WSM

Here we will discuss the applicability of our results to realistic Weyl materials. Specifically, our starting point is the following linearized model of a Weyl semimetal that preserves time-reversal symmetry but breaks inversion symmetry [77,78]. For simplicity, the tilting of the cones is considered only in one direction but the formalism can be generalized to

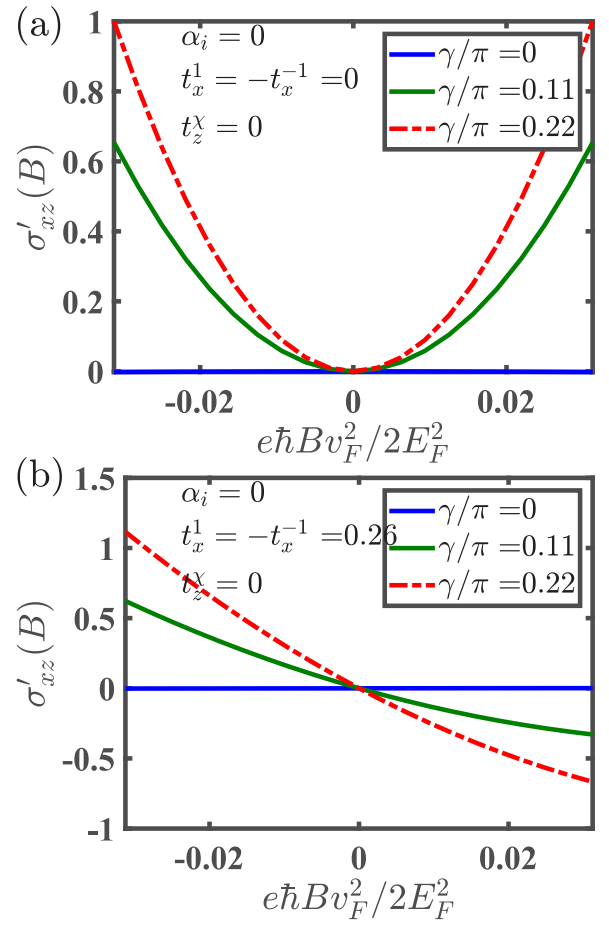


FIG. 12. Normalized planar Hall conductivity σ'_{xz} for oppositely tilted Weyl fermions along the x direction (prime indicates normalization with respect to magnetic field at 0.5 T). In the absence of intervalley scattering, a small tilt adds a linear-in- B component.

tilting in multiple directions as well:

$$H_{ib} = \sum_{n=1}^4 (\chi_n \hbar v_F \mathbf{k} \cdot \boldsymbol{\sigma} + \hbar v_F \gamma_n k_z \sigma_0). \quad (23)$$

The system consists of four Weyl nodes located at the points $\mathbf{K} = (\pm\pi/2, 0, \pm\pi/2)$ in the Brillouin zone. In the above Hamiltonian, χ_n is the chirality, and γ_n is the tilt. Specifically, $(\chi_1, \gamma_1) = (-\chi_2, \gamma_2) = (\chi_3, -\gamma_3) = (-\chi_4, -\gamma_4) = (-1, \gamma)$, and the tilt parameter γ is considered to be less than unity. This is also schematically represented in Fig. 14. We consider four intranode scattering channels (node $n \iff n$) and four internode scattering channels (node $n \iff n+1 \pmod{4}$), as also highlighted in Fig. 14. The internode scattering strength between node m and node n is β^{mn} . For simplicity, we neglect scattering between nodes $(4 \iff 2)$ and nodes $(1 \iff 3)$ since they involve a large momentum transfer. Intranode scattering at various nodes is qualitatively the same, while the internode scattering channels can be divided into two categories: (i) scattering between Weyl cones of opposite chirality and opposite tilt orientation $(1 \iff 2)$ and $(3 \iff 4)$, and (ii) scattering between Weyl cones of opposite chirality and same tilt orientation $(1 \iff 4)$ and $(2 \iff 3)$. Both of these cases have been discussed individually

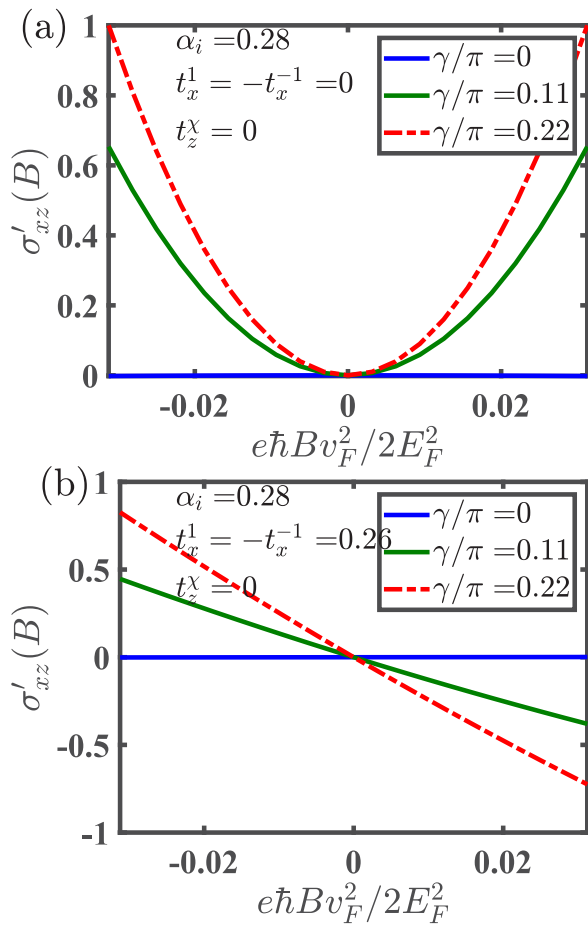


FIG. 13. Normalized planar Hall conductivity σ'_{xz} for oppositely tilted Weyl fermions along the k_x direction (prime indicates normalization with respect to magnetic field at 0.5 T). In the presence of intervalley scattering strength, the linear-in- B component is enhanced, but only in the presence of a finite tilt.

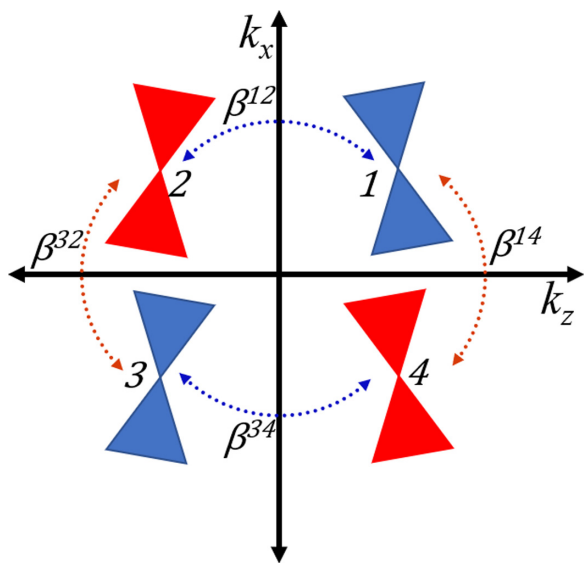


FIG. 14. Model for an inversion asymmetric Weyl semimetal with tilted Weyl cones. The colors of the Weyl cones are indicative of chirality. The parameters β^m indicate internode scattering between different nodes.

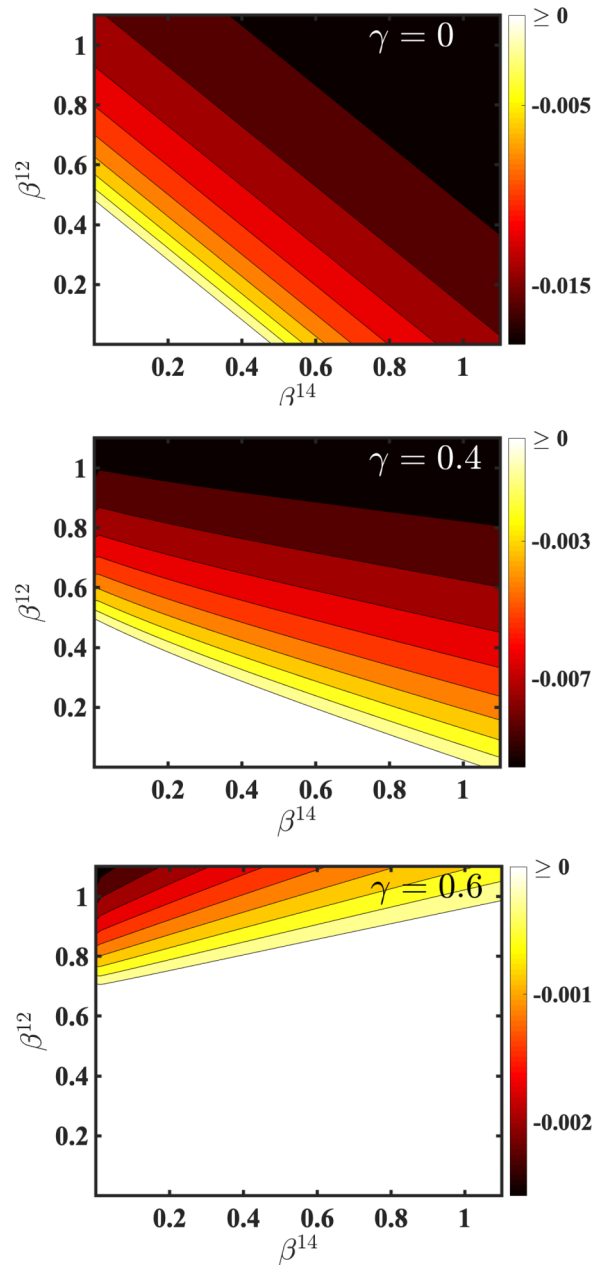


FIG. 15. LMC for inversion symmetry-broken WSM presented in Eq. (23) for different tilt values. The interplay of internode scatterings β^{12} and β^{14} along with the tilt parameter governs the sign of LMC. White region corresponds to positive LMC.

before, but here we consider the simultaneous effect of both categories.

In order to solve for the longitudinal magnetoconductance for this system, the formalism presented in Sec. II for two Weyl nodes is generalized to a system of multiple nodes as well with arbitrary values of tilt and chirality (see Appendix E). The solution to the Boltzmann equation for the system presented in Eq. (23) reduces to a system of 16 linear equations that are solved numerically for the unknown coefficients $\{\lambda^n, a^n, b^n, c^n\}$.

Interestingly, we find that despite the presence of internode scattering channels between cones of opposite tilt orientation,

the linear-in- B LMC vanishes. To understand this behavior we note from Fig. 4 that when tilt parameter changes sign ($t_z^1 \rightarrow -t_z^1$), the linear-in- B coefficient of LMC switches sign as well. From Fig. 14 we thus note that the linear-in- B coefficient generated by internode scattering channel ($1 \iff 2$) will be canceled by scattering channel ($4 \iff 3$). On the other hand the quadratic coefficient of LMC is an even function of the tilt parameter for all the scattering channels, making the behavior quadratic in magnetic field. From Figs. 6 and 4 we note that there is a quantitative difference in the quadratic coefficient for the two categories of internode scattering channel.

In Fig. 15 we plot the quadratic coefficient of the LMC (also corresponding to the sign of LMC) as a function of internode scattering strengths for different values of the tilt parameter γ . In the absence of any tilting, LMC is symmetric in β^{12} and β^{14} exhibiting a change of sign from positive to negative along a straight line contour from (0.5,0) to (0,0.5) in the $\beta^{12} - \beta^{14}$ parameter space. For nonzero values of tilt parameter the curve first stretches along the β^{14} axis and then along the β^{12} axis as per the expectations from Figs. 6 and 4. The interplay of internode scatterings and the tilt parameter governs the sign of LMC. In the limit of large tilt parameter the LMC sign remains positive.

IV. DISCUSSIONS AND CONCLUSIONS

The linearity or nonlinearity of the bands is alone not a sufficient criterion to produce a finite longitudinal magnetoconductance (positive or negative) or planar Hall effect in Weyl semimetals. In WSMs, it is in fact the topological nature of the bands that gives rise to finite LMC and PHE. The topological nature of the bands is manifest in the Berry curvature and the orbital magnetic moment of the Bloch electrons. Even though the bands no longer disperse linearly away from the Weyl node, their topology is nevertheless preserved, as also demonstrated by exact expressions for Berry curvature and OMM in our prototype lattice model. We solved the Boltzmann equation semianalytically for a lattice model of Weyl fermions and noted that the inclusion of orbital magnetic moment is crucial in obtaining negative LMC in the limit of vanishing intervalley scattering, just like it is crucial in obtaining negative LMC for strictly linearly dispersing Weyl fermions in the presence of intervalley scattering [71]. This points out to an important fact that nonlinear lattice effects can produce negative LMC for weak magnetic fields irrespective of the presence or absence of intervalley scattering. Therefore, it is inconclusive to state that negative LMC for weak magnetic fields in a Weyl semimetals necessarily points out to the presence of intervalley scattering.

Since nonlinear lattice effects are intrinsically present in real Weyl materials, likewise, the presence of a finite tilt is also inevitable. Finite lattice effects and effects due to tilting of the cones are largely independent of one another, and thus one can solve the Boltzmann equation for tilted Weyl fermions in the linearized approximation. The overall behavior is given by a combination of both factors. We constructed several phase diagrams in relevant parameter space that are important for diagnosing chiral anomaly in Weyl materials. Specifically, we examine the longitudinal magnetoconductivity σ_{zz} as well as the planar Hall conductivity σ_{xz} for tilted Weyl fermions for

the four relevant cases when the cones are tilted in the same or opposite direction along or perpendicular to the z direction, i.e., (i) $t_x^1 = t_x^{-1}$ and $t_z^1 = 0$, (ii) $t_x^1 = -t_x^{-1}$ and $t_z^1 = 0$, (iii) $t_z^1 = t_z^{-1}$ and $t_x^1 = 0$, (iv) $t_z^1 = -t_z^{-1}$ and $t_x^1 = 0$. Crucially, the LMC is found to depend on the angle γ that determines the orientation of the magnetic field with respect to the electric field. When $\gamma = \pi/2$, the electric and magnetic fields are parallel, and the LMC has a linear-in- B component only for case (iv) that results in its asymmetry around $B = 0$. We found that LMC when evaluated in the limit $B \rightarrow 0^+$ switches sign as a function of intervalley scattering α_i and the tilt parameter. For cases (i), (ii), and (iii), LMC is symmetric around $B = 0$ and quadratic in magnetic field, however, it changes sign from positive to negative depending on the magnitude of α_i and the tilt parameter. When $\gamma \neq \pi/2$, the phase plots for cases (i), (ii), and (iii) show nontrivial behavior. In particular, the distinction between cases (i) and (iii) becomes evident due to qualitatively different phase plots in the $\alpha_i - t_x$ space separating negative and positive LMC regions, which, however, is quadratic in magnetic field. Specifically, the shape of the zero-LMC contour is distinct in the two cases. Interestingly, for case (ii), a linear-in- B component in LMC is added that vanishes in the limit of parallel electric and magnetic fields. This again results in qualitative different phase plots in the $\alpha_i - t_z$ space as a function of γ . To summarize, the shape of the zero-LMC contour in $\alpha_i - t$ space as a function of the angle γ is qualitatively distinct in each of the four cases.

Next, we discussed the applicability of our results to a scenario much relevant to actual Weyl materials, i.e., the case of an inversion symmetry-broken Weyl semimetal by extending the Boltzmann formalism to tackle multiple nodes simultaneously. Interestingly, we find that despite the presence of internode scattering between nodes of opposite tilt orientation, the linear-in- B LMC coefficient vanishes for our model. We find that the interplay of various internode scattering channels along with the magnitude of tilt parameter governs the sign of LMC. Lastly, we also discuss the planar Hall conductivity σ_{xz} for each of the above cases. A linear-in- B component to σ_{xz} is added in cases (ii) and (iv), which is further enhanced by a finite α_i . The distinction between cases (ii) and (iv) comes from the fact that in addition to $\sin(2\gamma)$, a $\cos \gamma$ and a $\sin \gamma$ trend to the planar Hall conductivity is as a function of the angle γ for cases (iv) and (ii), respectively. The $\cos \gamma$ and $\sin \gamma$ trends are enhanced due to intervalley scattering.

ACKNOWLEDGMENTS

A.A. acknowledges support from IIT Mandi HTRA. G.S. acknowledges support from Grant No. IITM/SERB/GS/305.

APPENDIX A: LATTICE WEYL FERMION

The Hamiltonian of a Weyl node with smooth lattice cutoff can be expressed as

$$H^\chi = \chi E_0 \sin(\mathbf{ak} \cdot \boldsymbol{\sigma}), \quad (\text{A1})$$

where k is measured from the nodal point, χ is the chirality index, E_0 is an energy parameter, and a is constant with dimensions of length. Using the relations

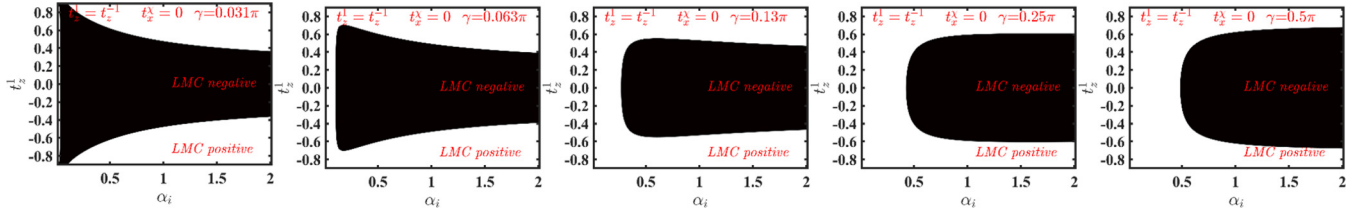


FIG. 16. Evolution of the phase diagram in the $t_z^1 - \alpha^i$ parameter space as a function of the angle of the magnetic field γ , when the Weyl cones are tilted along the same direction.

$\sin \theta = (\exp^{i\theta} - \exp^{-i\theta})/2i$ and $\exp\{ia(\boldsymbol{\sigma} \cdot \mathbf{k})\} = I \cos \theta + i(\boldsymbol{\sigma} \cdot \hat{\mathbf{k}}) \sin \theta$, one can rewrite the Hamiltonian in the following form (with θ and ϕ as polar and azimuthal angles, respectively):

$$H^\chi = \chi E_0 \sin(ak) \begin{pmatrix} \cos \theta & \sin \theta e^{-i\phi} \\ \sin \theta e^{i\phi} & -\cos \theta \end{pmatrix}. \quad (\text{A2})$$

Here we are going to use the property of matrices that for a matrix $M = [\dots]_{N \times N}$ having eigenvalues, $\lambda_1, \lambda_2, \lambda_3, \dots, \lambda_N$, and eigenfunctions $\alpha_1, \alpha_2, \alpha_3, \dots, \alpha_N$, respectively, then for matrix CM , the same will be $C\lambda_1, C\lambda_2, C\lambda_3, \dots, C\lambda_N$, and $\alpha_1, \alpha_2, \alpha_3, \dots, \alpha_N$ (where C is constant). Thus, the eigenvalues of the Hamiltonian are

$$\epsilon(\mathbf{k}) = \pm E_0 \sin(ak), \quad (\text{A3})$$

and eigenfunctions for positive band with different chirality are

$$|u^+(k)\rangle = \begin{pmatrix} e^{-i\phi} \cos \frac{\theta}{2} \\ \sin \frac{\theta}{2} \end{pmatrix}, \quad (\text{A4})$$

$$|u^-(k)\rangle = \begin{pmatrix} -e^{-i\phi} \sin \frac{\theta}{2} \\ \cos \frac{\theta}{2} \end{pmatrix}. \quad (\text{A5})$$

The expressions for Berry curvature and orbital magnetic moments (OMM) are given by

$$\Omega_{\mathbf{k}}^\chi = i \nabla_{\mathbf{k}} \times [\langle u^\chi(\mathbf{k}) | \nabla_{\mathbf{k}} | u^\chi(\mathbf{k}) \rangle],$$

$$m_{\mathbf{k}}^\chi = \frac{-ie}{2\hbar} \langle \nabla_{\mathbf{k}} u^\chi(\mathbf{k}) | \times [H^\chi(\mathbf{k}) - \epsilon(\mathbf{k})] | \nabla_{\mathbf{k}} u^\chi(\mathbf{k}) \rangle, \quad (\text{A6})$$

from which one can easily find the expressions for Berry curvature and OMM

$$\Omega_{\mathbf{k}}^\chi = \frac{-\chi \mathbf{k}}{2k^3},$$

$$m_{\mathbf{k}}^\chi = \frac{-e\chi E_0 \sin(ka)\mathbf{k}}{2\hbar k^3}. \quad (\text{A7})$$

APPENDIX B: BOLTZMANN TRANSPORT EQUATION

The Boltzmann equation is reduced to the form

$$\mathbb{Z} = \mathbb{A}\mathbb{Z} - \mathbb{Y}, \quad (\text{B1})$$

where

$$\mathbb{Z} = \begin{pmatrix} \lambda^+ \\ a^+ \\ b^+ \\ c^+ \\ \lambda^- \\ a^- \\ b^- \\ c^- \end{pmatrix} \quad (\text{B2})$$

$$\mathbb{A} = \begin{pmatrix} \alpha^{++}F^+ & \alpha^{++}G^+ & \alpha^{++}I^+ & \alpha^{++}J^+ & \alpha^{+-}F^- & \alpha^{+-}G^- & \alpha^{+-}I^- & \alpha^{+-}J^- \\ \alpha^{++}G^+ & \alpha^{++}O^+ & \alpha^{++}P^+ & \alpha^{++}Q^+ & \alpha^{+-}G^- & \alpha^{+-}O^- & \alpha^{+-}P^- & \alpha^{+-}Q^- \\ \alpha^{++}I^+ & \alpha^{++}P^+ & \alpha^{++}S^+ & \alpha^{++}U^+ & \alpha^{+-}I^- & \alpha^{+-}P^- & \alpha^{+-}S^- & \alpha^{+-}U^- \\ \alpha^{++}J^+ & \alpha^{++}Q^+ & \alpha^{++}U^+ & \alpha^{++}V^+ & \alpha^{+-}J^- & \alpha^{+-}Q^- & \alpha^{+-}U^- & \alpha^{+-}V^- \\ \alpha^{-+}F^+ & \alpha^{-+}G^+ & \alpha^{-+}I^+ & \alpha^{-+}J^+ & \alpha^{--}F^- & \alpha^{--}G^- & \alpha^{--}I^- & \alpha^{--}J^- \\ \alpha^{-+}G^+ & \alpha^{-+}O^+ & \alpha^{-+}P^+ & \alpha^{-+}Q^+ & \alpha^{--}G^- & \alpha^{--}O^- & \alpha^{--}P^- & \alpha^{--}Q^- \\ \alpha^{-+}I^+ & \alpha^{-+}P^+ & \alpha^{-+}S^+ & \alpha^{-+}U^+ & \alpha^{--}I^- & \alpha^{--}P^- & \alpha^{--}S^- & \alpha^{--}U^- \\ \alpha^{-+}J^+ & \alpha^{-+}Q^+ & \alpha^{-+}U^+ & \alpha^{-+}V^+ & \alpha^{--}J^- & \alpha^{--}Q^- & \alpha^{--}U^- & \alpha^{--}V^- \end{pmatrix}, \quad (\text{B3})$$

$$\mathbb{Y} = \begin{pmatrix} \alpha^{++}H^+ + \alpha^{+-}H^- \\ \alpha^{++}N^+ - \alpha^{+-}N^- \\ \alpha^{++}L^+ - \alpha^{+-}L^- \\ \alpha^{-+}M^+ - \alpha^{--}M^- \\ \alpha^{--}H^+ + \alpha^{-+}H^- \\ \alpha^{--}N^+ - \alpha^{-+}N^- \\ \alpha^{--}L^+ - \alpha^{-+}L^- \\ \alpha^{--}M^+ - \alpha^{-+}M^- \end{pmatrix}. \quad (\text{B4})$$

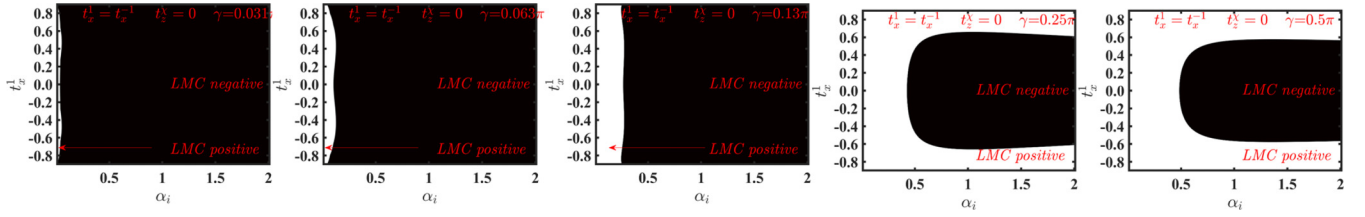


FIG. 17. Evolution of the phase diagram in the $t_x^1 - \alpha^i$ parameter space as a function of the angle of the magnetic field γ , when the Weyl cones are tilted along the same direction.

The relevant integrals involved in the above matrices are

$$\iint d\theta' d\phi' f^{X'}(\theta', \phi') = F^{X'}, \quad \iint d\theta' d\phi' f^{X'}(\theta', \phi') h^{X'} = H^{X'}, \quad (\text{B5})$$

$$\iint d\theta' d\phi' f^{X'}(\theta', \phi') \cos \theta' = G^{X'}, \quad \iint d\theta' d\phi' f^{X'}(\theta', \phi') \sin \theta' \cos \phi' = I^{X'}, \quad (\text{B6})$$

$$\iint d\theta' d\phi' f^{X'}(\theta', \phi') \sin \theta' \sin \phi' = J^{X'}, \quad \iint d\theta' d\phi' f^{X'}(\theta', \phi') \sin^2 \theta' \cos^2 \phi' = S^{X'}, \quad (\text{B7})$$

$$\iint d\theta' d\phi' f^{X'}(\theta', \phi') h^{X'}(\theta', \phi') \cos \theta' = N^{X'}, \quad \iint d\theta' d\phi' f^{X'}(\theta', \phi') h^{X'}(\theta', \phi') \sin \theta' \cos \phi' = L^{X'}, \quad (\text{B8})$$

$$\iint d\theta' d\phi' f^{X'}(\theta', \phi') h^{X'}(\theta', \phi') \sin \theta' \sin \phi' = M^{X'}, \quad \iint d\theta' d\phi' f^{X'}(\theta', \phi') \cos^2 \theta' = O^{X'}, \quad (\text{B9})$$

$$\iint d\theta' d\phi' f^{X'}(\theta', \phi') \sin \theta' \cos \theta' \cos \phi' = P^{X'}, \quad \iint d\theta' d\phi' f^{X'}(\theta', \phi') \sin \theta' \cos \theta' \sin \phi' = Q^{X'}, \quad (\text{B10})$$

$$\iint d\theta' d\phi' f^{X'}(\theta', \phi') \sin^2 \theta' \cos \phi' \sin \phi' = U^{X'}, \quad \iint d\theta' d\phi' f^{X'}(\theta', \phi') \sin^2 \theta' \sin^2 \phi' = V^{X'}. \quad (\text{B11})$$

APPENDIX C: EVOLUTION OF THE LMC PHASE DIAGRAM WITH MAGNETIC FIELD

In Fig. 16 we plot the evolution of the contour shape in the $t_x^1 - \alpha^i$ parameter space as a function of the angle of the magnetic field γ . When γ is directed away from $\pi/2$ the shape of the zero LMC contour looks like a curved trapezoid instead of U . The critical value α_i^c where the sign change first occurs is seen to reduce and elongate its region from $|t_z| \approx 0.5$ when $\gamma = \pi/2$ to $|t_z| \approx 1$ as $\gamma \rightarrow 0$. In Fig. 17 we plot the evolution of the contour shape in the $t_x^1 - \alpha^i$ parameter space as a function of the angle of the magnetic field γ . It is noted that region of negative LMC expands in the parameter space along with the reduction of the critical intervalley strength α_i^c where the sign change first occurs. The reduction of the critical intervalley strength can again be understood as a combination of the two factors (i) a finite tilt and intervalley scattering (when $\gamma = \pi/2$) drives the system to change the LMC sign from

positive to negative, and second directing the magnetic field away from the z axis in the presence of intervalley scattering (in the absence of tilt) drives the system to change LMC sign from positive to negative much below the critical intervalley strength. The different shape of the contour (negative LMC filling out the parameter space instead of a curved trapezoid) is essentially because the cones are now tilted along the x direction and the magnetic field has an x component to it, which is qualitatively different from the tilt occurring in the z direction. Finally, in Fig. 18 we plot the evolution of the phase diagram when the Weyl cones are tilted along the x direction but oriented opposite to each other. Directing the magnetic field even slightly away from the z axis changes the qualitative behavior since a linear-in- B component is added in the LMC response. This is because the magnetic field now has a finite component along the tilt direction, and the tilts are oppositely oriented to each other.

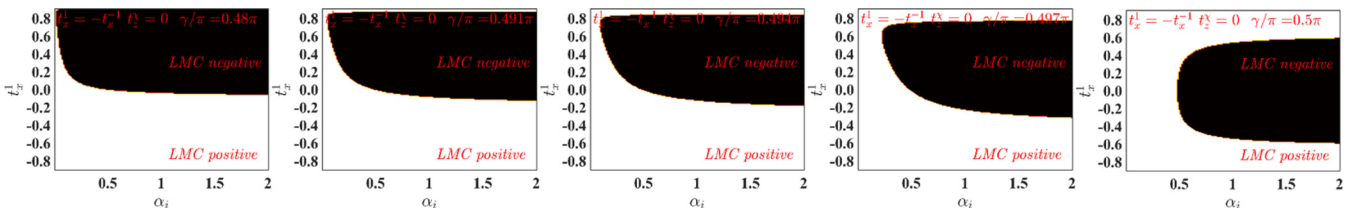


FIG. 18. Evolution of the phase diagram in the $t_x^1 - \alpha^i$ parameter space as a function of the angle of the magnetic field γ , when the Weyl cones are tilted opposite to each other.

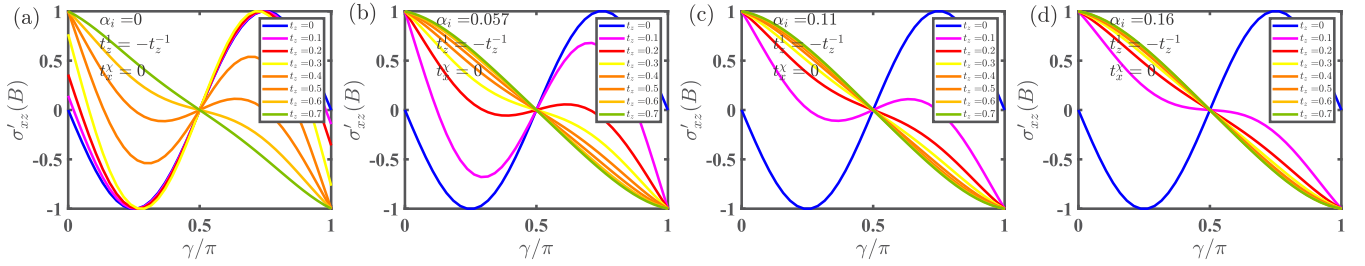


FIG. 19. Normalized planar Hall conductivity (σ'_{xz}) as a function of the angle γ for several values of tilt parameter t_z for oppositely tilted Weyl cones. In the absence of tilt the behavior follows the trend $\sin(2\gamma)$, while in the presence of tilt, a $\cos \gamma$ component is added. Beyond a critical t_z^c , the $\cos \gamma$ term dominates and $\sigma'_{xz}(\pi/2 + \epsilon)$ changes from positive to negative, where ϵ is a small positive angle. A finite intervalley scattering further enhances the $\cos \gamma$ trend (however, only in the presence of a finite tilt). Its effect is to lower the critical tilt t_z^c where the sign change occurs.

APPENDIX D: ANGULAR DEPENDENCE ON PHC

In Fig. 19 we plot the normalized planar Hall conductivity (σ'_{xz}) as a function of the angle γ for several values of tilt parameter t_z for oppositely tilted Weyl cones. In the absence of tilt the behavior follows the trend $\sin(2\gamma)$, while in the presence of tilt, a $\cos \gamma$ component is added. Beyond a critical t_z^c , the $\cos \gamma$ term dominates and $\sigma'_{xz}(\pi/2 + \epsilon)$ changes from positive to negative, where ϵ is a small positive angle. A finite intervalley scattering further enhances the $\cos \gamma$ trend (however, only in the presence of a finite tilt). Its effect is to lower the critical tilt t_z^c where the sign change occurs.

In Fig. 20 we plot the normalized planar Hall conductivity as a function of the angle γ for several values of tilt parameter t_x for oppositely tilted Weyl cones. In the absence of tilt, the behavior follows the expected trend of $\sin(2\gamma)$, while in the presence of tilt, a $\sin \gamma$ component is added. Beyond a critical value of the tilt (t_x^c), the $\sin \gamma$ term dominates the behavior σ'_{xz} never changes sign as a function of the parameter γ . A finite intervalley scattering further enhances the $\sin \gamma$ trend (however, only in the presence of a finite tilt). Its effect is to lower the critical value of the tilt t_x^c .

APPENDIX E: BOLTZMANN TRANSPORT FOR A SYSTEM WITH MULTIPLE NODES

For a system with multiple Weyl nodes, the distribution function at each node can be represented by $f_{\mathbf{k}}^m$. Generalizing the formalism presented in the main text, the collision inte-

gral must take into account scattering between multiple Weyl cones that may or may not be of the same chirality or tilt. Thus, $\mathcal{I}_{\text{col}}[f_{\mathbf{k}}^m]$ can be expressed as

$$\mathcal{I}_{\text{col}}[f_{\mathbf{k}}^m] = \sum_p \sum_{\mathbf{k}'} W_{\mathbf{k},\mathbf{k}'}^{mp} (f_{\mathbf{k}'}^p - f_{\mathbf{k}}^m), \quad (\text{E1})$$

where the sum p runs over nodes, and scattering rate $W_{\mathbf{k},\mathbf{k}'}^{mp}$ in the first Born approximation is given by

$$W_{\mathbf{k},\mathbf{k}'}^{mp} = \frac{2\pi}{\hbar} \frac{n}{\mathcal{V}} |\langle \psi_{\mathbf{k}'}^p | U_{\mathbf{k}\mathbf{k}'}^{mp} | \psi_{\mathbf{k}}^m \rangle|^2 \delta(\epsilon_{\mathbf{k}'}^p - \epsilon_{\mathbf{k}}^m). \quad (\text{E2})$$

The scattering potential profile $U_{\mathbf{k}\mathbf{k}'}^{mp}$ can be chosen such that scattering between all or some of the nodes (internode) as well as within each node (intranode) is considered. Proceeding as before, we define the valley scattering time $\tau_{\mathbf{k}}^m$ as

$$\frac{1}{\tau_{\mathbf{k}}^m(\theta, \phi)} = \mathcal{V} \sum_p \iint \frac{\beta^{mp}(k')^3}{|\mathbf{v}_{\mathbf{k}'}^p \cdot \mathbf{k}'^p|} \sin \theta' \mathcal{G}^{mp}(\mathcal{D}_{\mathbf{k}'}^p)^{-1} d\theta' d\phi', \quad (\text{E3})$$

and the Boltzmann equation becomes

$$\begin{aligned} h_{\mu}^m(\theta, \phi) + \frac{\Lambda_{\mu}^m(\theta, \phi)}{\tau_{\mu}^m(\theta, \phi)} \\ = \mathcal{V} \sum_p \iint \frac{\beta^{mp}(k')^3}{|\mathbf{v}_{\mathbf{k}'}^p \cdot \mathbf{k}'^p|} \sin \theta' \mathcal{G}^{mp}(\mathcal{D}_{\mathbf{k}'}^p)^{-1} \Lambda_{\mu}^p(\theta', \phi') d\theta' d\phi'. \end{aligned} \quad (\text{E4})$$

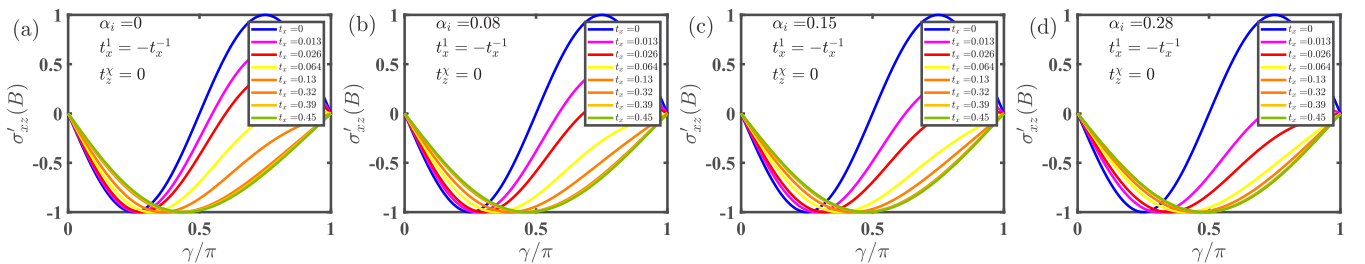


FIG. 20. Normalized planar Hall conductivity (σ'_{xz}) as a function of the angle γ for several values of tilt parameter t_x for oppositely tilted Weyl cones. In the absence of tilt the behavior follows the trend $\sin(2\gamma)$, while in the presence of tilt, a $\sin \gamma$ component is added. Beyond a critical t_x^c , the $\sin \gamma$ term dominates and $\sigma'_{xz}(\pi/2 + \epsilon)$ changes from positive to negative, where ϵ is a small positive angle. A finite intervalley scattering further enhances the $\sin \gamma$ trend (however, only in the presence of a finite tilt). Its effect is to lower the critical tilt t_x^c where the sign change occurs.

Making the ansatz $\Lambda_\mu^m(\theta, \phi) = [\lambda^m - h_\mu^m(\theta, \phi) + a^m \cos \theta + b^m \sin \theta \cos \phi + c^m \sin \theta \sin \phi] \tau_\mu^m(\theta, \phi)$, and using the particle-number conservation constraint, the Boltzmann

equation is reduced to a system of $4N$ equations to be solved for $4N$ unknowns (N being the number of nodes).

-
- [1] J. von Neumann and E. Wigner, *Z. Phys.* **30**, 467 (1929).
- [2] G. E. Volovik, *The Universe in a Helium Droplet*, Vol. 117 (Oxford University Press, Oxford, 2003).
- [3] C.-K. Chiu, J. C. Y. Teo, A. P. Schnyder, and S. Ryu, *Rev. Mod. Phys.* **88**, 035005 (2016).
- [4] N. P. Armitage, E. J. Mele, and A. Vishwanath, *Rev. Mod. Phys.* **90**, 015001 (2018).
- [5] S.-Y. Yang, H. Yang, E. Derunova, S. S. Parkin, B. Yan, and M. N. Ali, *Adv. Phys.: X* **3**, 1414631 (2018).
- [6] S. Murakami, *New J. Phys.* **9**, 356 (2007).
- [7] S. Murakami, S. Iso, Y. Avishai, M. Onoda, and N. Nagaosa, *Phys. Rev. B* **76**, 205304 (2007).
- [8] A. A. Burkov, M. D. Hook, and L. Balents, *Phys. Rev. B* **84**, 235126 (2011).
- [9] A. A. Burkov and L. Balents, *Phys. Rev. Lett.* **107**, 127205 (2011).
- [10] X. Wan, A. M. Turner, A. Vishwanath, and S. Y. Savrasov, *Phys. Rev. B* **83**, 205101 (2011).
- [11] G. Xu, H. Weng, Z. Wang, X. Dai, and Z. Fang, *Phys. Rev. Lett.* **107**, 186806 (2011).
- [12] K.-Y. Yang, Y.-M. Lu, and Y. Ran, *Phys. Rev. B* **84**, 075129 (2011).
- [13] D. Xiao, M.-C. Chang, and Q. Niu, *Rev. Mod. Phys.* **82**, 1959 (2010).
- [14] A. A. Burkov, *Phys. Rev. Lett.* **113**, 187202 (2014).
- [15] G. Sharma, P. Goswami, and S. Tewari, *Phys. Rev. B* **93**, 035116 (2016).
- [16] G. Sharma, C. Moore, S. Saha, and S. Tewari, *Phys. Rev. B* **96**, 195119 (2017).
- [17] T. Liang, J. Lin, Q. Gibson, T. Gao, M. Hirschberger, M. Liu, R. J. Cava, and N. P. Ong, *Phys. Rev. Lett.* **118**, 136601 (2017).
- [18] S. L. Adler, *Phys. Rev.* **177**, 2426 (1969).
- [19] H. B. Nielsen and M. Ninomiya, No-go theorem for regularizing chiral fermions, Science Research Council, Technical Report, 1981 (unpublished).
- [20] H. B. Nielsen and M. Ninomiya, *Phys. Lett. B* **130**, 389 (1983).
- [21] J. S. Bell and R. Jackiw, *Il Nuovo Cimento A (1965-1970)* **60**, 47 (1969).
- [22] V. Aji, *Phys. Rev. B* **85**, 241101(R) (2012).
- [23] A. A. Zyuzin, S. Wu, and A. A. Burkov, *Phys. Rev. B* **85**, 165110 (2012).
- [24] D. T. Son and N. Yamamoto, *Phys. Rev. Lett.* **109**, 181602 (2012).
- [25] P. Goswami and S. Tewari, *Phys. Rev. B* **88**, 245107 (2013).
- [26] P. Goswami, G. Sharma, and S. Tewari, *Phys. Rev. B* **92**, 161110(R) (2015).
- [27] K. Fukushima, D. E. Kharzeev, and H. J. Warringa, *Phys. Rev. D* **78**, 074033 (2008).
- [28] D. T. Son and B. Z. Spivak, *Phys. Rev. B* **88**, 104412 (2013).
- [29] K.-S. Kim, H.-J. Kim, and M. Sasaki, *Phys. Rev. B* **89**, 195137 (2014).
- [30] V. A. Zyuzin, *Phys. Rev. B* **95**, 245128 (2017).
- [31] L. P. He, X. C. Hong, J. K. Dong, J. Pan, Z. Zhang, J. Zhang, and S. Y. Li, *Phys. Rev. Lett.* **113**, 246402 (2014).
- [32] T. Liang, Q. Gibson, M. N. Ali, M. Liu, R. J. Cava, and N. P. Ong, *Nat. Mater.* **14**, 280 (2015).
- [33] C.-L. Zhang, S.-Y. Xu, I. Belopolski, Z. Yuan, Z. Lin, B. Tong, G. Bian, N. Alidoust, C.-C. Lee, S.-M. Huang *et al.*, *Nat. Commun.* **7**, 1 (2016).
- [34] Q. Li, D. E. Kharzeev, C. Zhang, Y. Huang, I. Pletikosić, A. Fedorov, R. Zhong, J. Schneeloch, G. Gu, and T. Valla, *Nat. Phys.* **12**, 550 (2016).
- [35] J. Xiong, S. K. Kushwaha, T. Liang, J. W. Krizan, M. Hirschberger, W. Wang, R. J. Cava, and N. P. Ong, *Science* **350**, 413 (2015).
- [36] M. Hirschberger, S. Kushwaha, Z. Wang, Q. Gibson, S. Liang, C. A. Belvin, B. A. Bernevig, R. J. Cava, and N. P. Ong, *Nat. Mater.* **15**, 1161 (2016).
- [37] S. Nandy, G. Sharma, A. Taraphder, and S. Tewari, *Phys. Rev. Lett.* **119**, 176804 (2017).
- [38] N. Kumar, S. N. Guin, C. Felser, and C. Shekhar, *Phys. Rev. B* **98**, 041103(R) (2018).
- [39] J. Yang, W. L. Zhen, D. D. Liang, Y. J. Wang, X. Yan, S. R. Weng, J. R. Wang, W. Tong, L. Pi, W. K. Zhu, and C. J. Zhang, *Phys. Rev. Materials* **3**, 014201 (2019).
- [40] H. Li, H.-W. Wang, H. He, J. Wang, and S.-Q. Shen, *Phys. Rev. B* **97**, 201110(R) (2018).
- [41] F. C. Chen, X. Luo, J. Yan, Y. Sun, H. Y. Lv, W. J. Lu, C. Y. Xi, P. Tong, Z. G. Sheng, X. B. Zhu, W. H. Song, and Y. P. Sun, *Phys. Rev. B* **98**, 041114(R) (2018).
- [42] P. Li, C. H. Zhang, J. W. Zhang, Y. Wen, and X. X. Zhang, *Phys. Rev. B* **98**, 121108(R) (2018).
- [43] J. Yang, J. R. Wang, W. L. Zhen, L. Ma, L. S. Ling, W. Tong, C. J. Zhang, L. Pi, and W. K. Zhu, *Phys. Rev. B* **100**, 205107 (2019).
- [44] O. Pavlosiuk, D. Kaczorowski, and P. Wiśniewski, *Phys. Rev. B* **99**, 125142 (2019).
- [45] R. Singha, S. Roy, A. Pariari, B. Satpati, and P. Mandal, *Phys. Rev. B* **98**, 081103(R) (2018).
- [46] R. Lundgren, P. Laurell, and G. A. Fiete, *Phys. Rev. B* **90**, 165115 (2014).
- [47] G. Sharma and S. Tewari, *Phys. Rev. B* **100**, 195113 (2019).
- [48] K. Das and A. Agarwal, *Phys. Rev. B* **100**, 085406 (2019).
- [49] A. L. Levy, A. B. Sushkov, F. Liu, B. Shen, N. Ni, H. D. Drew, and G. S. Jenkins, *Phys. Rev. B* **101**, 125102 (2020).
- [50] J.-M. Parent, R. Côté, and I. Garate, *Phys. Rev. B* **102**, 245126 (2020).
- [51] S. A. Parameswaran, T. Grover, D. A. Abanin, D. A. Pesin, and A. Vishwanath, *Phys. Rev. X* **4**, 031035 (2014).
- [52] Z. Song, J. Zhao, Z. Fang, and X. Dai, *Phys. Rev. B* **94**, 214306 (2016).
- [53] P. Rinkel, P. L. S. Lopes, and I. Garate, *Phys. Rev. Lett.* **119**, 107401 (2017).
- [54] X. Yuan, C. Zhang, Y. Zhang, Z. Yan, T. Lyu, M. Zhang, Z. Li, C. Song, M. Zhao, P. Leng *et al.*, *Nat. Commun.* **11**, 1 (2020).

- [55] B. Cheng, T. Schumann, S. Stemmer, and N. Armitage, [arXiv:1910.13655](#).
- [56] P. Goswami, J. H. Pixley, and S. Das Sarma, *Phys. Rev. B* **92**, 075205 (2015).
- [57] H.-Z. Lu, S.-B. Zhang, and S.-Q. Shen, *Phys. Rev. B* **92**, 045203 (2015).
- [58] C.-Z. Chen, H. Liu, H. Jiang, and X. C. Xie, *Phys. Rev. B* **93**, 165420 (2016).
- [59] S.-B. Zhang, H.-Z. Lu, and S.-Q. Shen, *New J. Phys.* **18**, 053039 (2016).
- [60] J. Shao and L. Yan, *AIP Adv.* **9**, 045319 (2019).
- [61] X. Li, B. Roy, and S. Das Sarma, *Phys. Rev. B* **94**, 195144 (2016).
- [62] X.-T. Ji, H.-Z. Lu, Z.-G. Zhu, and G. Su, *J. Appl. Phys.* **123**, 203901 (2018).
- [63] B. Z. Spivak and A. V. Andreev, *Phys. Rev. B* **93**, 085107 (2016).
- [64] K. Das and A. Agarwal, *Phys. Rev. B* **99**, 085405 (2019).
- [65] M. Imran and S. Hershfield, *Phys. Rev. B* **98**, 205139 (2018).
- [66] R. M. Dantas, F. Peña-Benitez, B. Roy, and P. Surówka, *J. High Energy Phys.* **12** (2018) 069.
- [67] A. Johansson, J. Henk, and I. Mertig, *Phys. Rev. B* **99**, 075114 (2019).
- [68] A. G. Grushin, J. W. F. Venderbos, A. Vishwanath, and R. Ilan, *Phys. Rev. X* **6**, 041046 (2016).
- [69] A. Cortijo, *Phys. Rev. B* **94**, 241105(R) (2016).
- [70] G. Sharma, P. Goswami, and S. Tewari, *Phys. Rev. B* **96**, 045112 (2017).
- [71] A. Knoll, C. Timm, and T. Meng, *Phys. Rev. B* **101**, 201402(R) (2020).
- [72] C. Xiao, H. Chen, Y. Gao, D. Xiao, A. H. MacDonald, and Q. Niu, *Phys. Rev. B* **101**, 201410(R) (2020).
- [73] G. Sharma, S. Nandy, and S. Tewari, *Phys. Rev. B* **102**, 205107 (2020).
- [74] A. A. Soluyanov, D. Gresch, Z. Wang, Q. Wu, M. Troyer, X. Dai, and B. A. Bernevig, *Nature (London)* **527**, 495 (2015).
- [75] S. Rostamzadeh, I. Adagideli, and M. O. Goerbig, *Phys. Rev. B* **100**, 075438 (2019).
- [76] H. Bruus and K. Flensberg, *Many-body Quantum Theory in Condensed Matter Physics: An Introduction* (Oxford University Press, Oxford, 2004).
- [77] T. M. McCormick, I. Kimchi, and N. Trivedi, *Phys. Rev. B* **95**, 075133 (2017).
- [78] S. Bertrand, J.-M. Parent, R. Côté, and I. Garate, *Phys. Rev. B* **100**, 075107 (2019).